Spring 1998

The Effects of Fabry-Perot Fringing on the Sensitivity of a Wavelength Modulation Experiment

Patrick C. Shea
Old Dominion University

THE EFFECTS OF FABRY-PEROT FRINGING ON THE SENSITIVITY OF A WAVELENGTH MODULATION EXPERIMENT

by

Patrick C. Shea
B.S.E.E. May 1997, Old Dominion University

A Thesis submitted to the Faculty of Old Dominion University in Partial Fulfillment of the Requirement for the Degree of

MASTER OF SCIENCE
ELECTRICAL ENGINEERING

OLD DOMINION UNIVERSITY
May 1998

Approved by:

_____
Dr. Amin N. Dharamsi (Director)

_____
Dr. William Chu (NASA Langley Research Center)

_____
Dr. Glenn Gerdin (Member)

ABSTRACT
THE EFFECTS OF FABRY-PEROT FRINGING ON THE SENSITIVITY OF A WAVELENGTH MODULATION EXPERIMENT

Patrick C. Shea

Old Dominion University, 1998
Director: Dr. Amin N. Dharamsi

Parasitic Fabry-Perot etaloning plagues many experiments which use wavelength modulation spectroscopy. This fringing, which is an artifact that almost always appears in such experiments, arises from multiple reflections in the optical elements in the experimental apparatus. The etaloning plays a detrimental role and limits the ultimate sensitivity of wavelength modulation spectroscopy experiments. The research described in this thesis investigates this phenomenon. Experimental results are presented which show that when the Q-factor of the parasitic etalon is smaller that that of the absorption line being measured, significant improvement in the Signal to Fringe Noise Ratio can be obtained through the use of higher harmonic detection.

A model is developed and experimental results are compared with theoretical predictions. The extremely good agreement obtained enables us to extract accurate values for the modeling parameters. Line centers, line widths, and optical absorption cross-sections of several lines in the oxygen A-band are measured with high accuracy using the etalon as a reference.

ACKNOWLEDGEMENTS

I would like to thank Dr. Dharamsi for devoting two years of his time toward guiding and assisting me in the completion of my Masters degree in Electrical Engineering. Without his direction I would never have made it to this point in my educational career.

I would like to gratefully acknowledge the financial support provided by a NASA Graduate Student Researcher Program (GSRP) fellowship that allowed me to attend graduate school and focus on my research. Dr. William P. Chu's assistance was especially important.

I also wish to thank Audra Bullock for all of her assistance in the laboratory. Her continual reassurance and support really made a difference and kept me progressing toward my goal of completing this research.

To my parents, George and Eileen Shea, I give a special thanks for the many years of support and guidance that they have given me throughout my educational career.

To Pam, thanks for her support, compassion, and understanding always, and in particular, during the times when everything might not have been progressing quite as smoothly in the laboratory as I might have wished.

TABLE OF CONTENTS

LIST OF TABLES

LIST OF FIGURES

CHAPTER I

INTRODUCTION

Wavelength modulation spectroscopy is a useful non-intrusive measuring tool that has been used for many years to measure gaseous density, temperature, and velocity. This technique is superior to normal spectroscopy because of a substantial increase in the signal to noise ratio that results by modulating the signal and using phase-sensitive detection at the modulation frequency or at one of its harmonics.

One source of noise that plagues wavelength modulation spectroscopy experiments is fringing. Fringing arises because of the presence of parallel reflective surfaces in the experimental apparatus. Often this fringing is due to optical blanks such as the windows of a chamber containing the sample gas. Fringing is also introduced by scattering within multipass cells; particularly the White cell [1]. There have been attempts to eliminate the fringing introduced by multipass cells by several groups. One such group overcame the problem by jittering one of the mirrors in the multipass cell [1]. Silver and Stanton attached a piezoelectric transducer (PZT) to one of the mirrors in their multipass cell and oscillated the mirror along the optical axis at a frequency asynchronous with any other modulation frequency used in the experiment. They found that if the mirror was moved over a distance greater than one half of the free spectral range of the fringe, which is approximately $\lambda/4$, then the fringing would average out to zero over one scan [1]. In the actual experiment, the mirror was oscillated over several wavelengths so sufficient jittering was done to reduce the effects of fringing.

Journal of Applied Physics

Another method for eliminating fringing in multipass cells was presented by Fried, et al. [2]. Their approach was to modulate the pressure of the gas contained in the cell. Their results show an increase in signal to noise ratio greater than that obtained by Silver and Stanton. The modulation pressure was on the order of 10 torr on a 25 torr base pressure. However, this method is limited by the fact that the pressure cannot be modulated rapidly [2].

An uncommon, but increasingly popular use of higher harmonic detection has recently been proven to be advantageous in many applications. The use of higher order harmonics results in more sensitive measurements of gaseous density fluctuations [3]. Higher order harmonic detection also allows resolution of overlapping lines which otherwise may appear as a single line [4]. This thesis shows that higher harmonic detection also results in a reduction in the Fabry-Perot fringing measured in the experiment. This is possible due to the derivative like properties observed in wavelength modulation signals [5]. The derivatives of the functions amplify the slopes of the signal, and since the absorption signal generally has a larger slope than the transmission function of the parasitic Fabry-Perot etalon, the signal to fringing noise ratio tends to increase with increasing harmonic detection order.

Since the experimental work done in this thesis is on the oxygen A-band lines, a brief discussion of the spectroscopy of O_2 is given in Chapter II, Section 1. This is followed by a review of lineshape functions, which are used to theoretically calculate the absorption profile. Since the accuracy of these lineshape functions is one factor that determines the accuracy to which the line parameters can be extracted from the experimental data, a good understanding of the profile is important. Also included in

Chapter II is a discussion of the usefulness of modulation spectroscopy in the measurement of concentration, temperature, and velocity of gaseous media. Chapter III contains a derivation of the equations used to model Fabry-Perot fringing in a wavelength modulation experiment. Also included in Chapter III is a theoretical study of the etalon parameters on the resulting transmission function. The experimental results and discussion is contained in Chapter IV. The thesis is concluded in Chapter V with a final discussion of Fabry-Perot fringing and a proposal into ways to exploit the fringing and make turn it into an advantage.

CHAPTER II

BACKGROUND ON WAVELENGTH MODULATION SPECTROSCOPY

The work described in this thesis was performed among lines of the A-band of molecular oxygen. This absorption band, in the 760 nanometer region of the spectrum, was investigated in the mid-eighties by Ritter and Wilkerson [6]. There is however a need to verify some of the line parameters they obtained, as well as to fill in some of the gaps in their data.

This chapter gives background information on the absorption spectrum of oxygen as well as on other related issues dealing with wavelength modulation spectroscopy. Determination of the line parameters requires, amongst other things, an accurate theoretical modeling of the absorption line profile. Hence, Section 2.2 discusses issues related to the lineshape function. This chapter concludes with a section discussing uses of wavelength modulation spectroscopy in measuring density, velocity, temperature, and fluctuations of any of these parameters.

2.1 The Absorption Spectrum of Oxygen

The absorption lines studied in this research are contained in the oxygen A-band. The A-band is one of four bands in the absorption spectrum of oxygen. These bands are denoted as A, B, γ, and δ, and correspond to (0 ← 0), (1 ← 0), (2 ← 0), and (3 ← 0) vibrational transitions of the $b^1\Sigma_g^+ \leftarrow X^3\Sigma_g^-$ electronic transition of molecular oxygen [6]. The electronic states for oxygen are shown in Figure 1 [8]. The individual absorption lines are named using their energy quantum numbers. The quantum numbers J and K are used to designate the states of the rotational levels. J represents the total angular

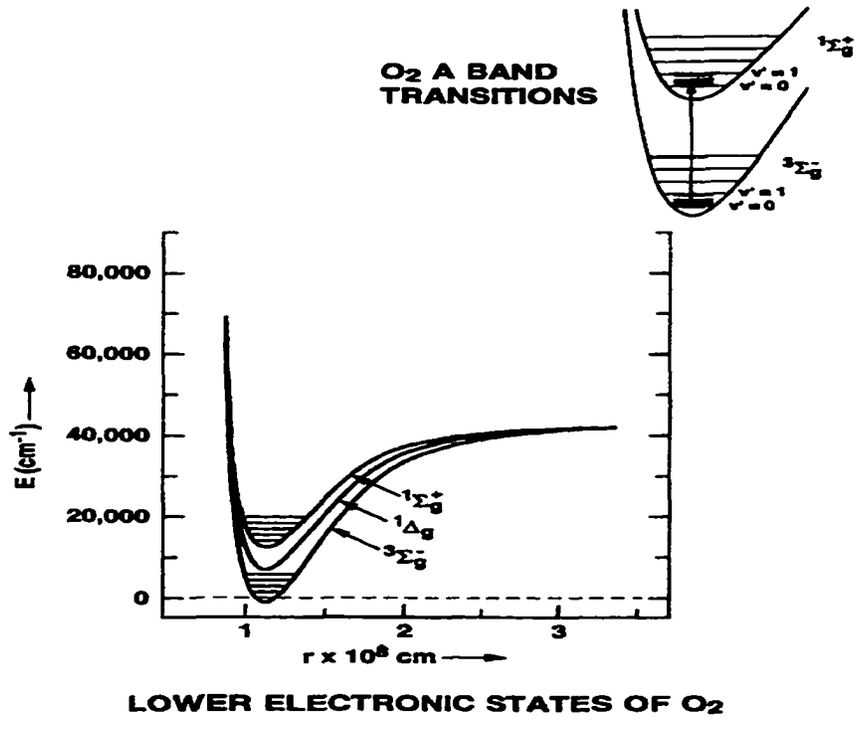

Figure 1 Some low-lying electronic states of the oxygen molecule. The insert shows the A-Band transitions.

momentum of the state, and K represents the state's rotational angular momentum. The total angular momentum, J, is the sum of the rotational angular momentum, K, and the spin angular momentum, S (i.e. J=K+S). The general spectroscopic notation of an absorption line is: $\Delta K \Delta J(K'', J'')$, where ΔK is the net change in the rotational angular momentum (i.e. $\Delta K = K' - K''$), J is the net change in the total angular momentum. K" is the lower state rotational angular momentum, and J" is the lower state total angular momentum. The only allowable values for ΔK and ΔJ are -1, 0, and +1 which are represented by P, Q and R respectively [6]. For example, a typical line in the Oxygen A band that is studied in the laboratory is RQ(13,14). This line corresponds to a transition between two states; the lower one having a rotational angular momentum quantum number 13 (K"=13) and total angular momentum quantum number 14 (J"=14). The upper state has quantum numbers K'=14 and J'=13.

The oxygen A-band consists of very weak absorption lines. In most molecules, electrons change energy states when tuned light is incident on them because the latter act like quantum mechanical receiving electric dipole antennas: there is a different wave function for each energy level E_1 and E_2 denoted by ψ_1 and ψ_2 respectively. During a radiative transition the wave functions ψ_1 and ψ_2 interfere with one another. It can be shown that this interference between ψ_1 and ψ_2 creates a charge oscillator which oscillates at a frequency of $\nu=(E_2-E_1)/h$. This means that a photon of frequency ν, which has energy of $h\nu$, will cause an electron to jump to the higher energy level. In oxygen the symmetric properties of the wave functions result in there being no electric dipole moment. However Maxwell's equations show that radiative transitions can also occur when magnetic dipole moments change. The oxygen A-band transition utilizes such a magnetic dipole moment change. However, since the probability of a magnetic dipole transition is much smaller than that for an electric dipole transition, the resulting absorption spectrum is quite weak [8].

In addition, the electronic transition in oxygen relevant to the A-band is one in which the spin changes during the transition between energy states. The lower state in oxygen, $X^3\Sigma_g^-$, is a triplet denoted by the multiplicity of 3. This means that the energy level splits into three levels in the presence of a magnetic field because the total spin of the electrons is 1. The upper state for an A-band transition, $b^1\Sigma_g^+$, is a singlet denoted by the 1 corresponding to a total spin, s, of zero [9]. (The multiplicity of a state is given by 2s+1.) Hence in order for a transition to occur, the electron must change its spin, which is a low probability event. Due to this condition on the A-band transitions, they are termed

"spin forbidden transitions." The probability for a spin forbidden transition is also very small. This, coupled with the fact that the transition only draws its strength from a magnetic dipole change, produces an extremely weak absorption line. These transitions are 10^{-6} to 10^{-8} times less likely to occur than the more common spin-allowed electric dipole transition [9].

In order to interpret data collected in any absorption experiment, a theoretical lineshape profile must be used to model the line. Characteristics such as line strength, line width, and line broadening parameters are all used in modeling an absorption line and give information about the line.

2.2 Lineshape Functions

The lineshape function is generally denoted by, $g(\nu)$, and describes the profile of the absorption line in the frequency domain. Mathematically, $g(\nu)d\nu$ is the probability that a radiative transition occurs involving a photon of frequency between ν and $\nu+d\nu$. Consequently, the normalization condition holds i.e. $\int_0^\infty g(\nu)d\nu = 1$. By precisely measuring the absorption signal, the shape of the profile can yield many properties of the sample gas. These properties are specie type, concentration or density, velocity, and temperature [10].

The lineshape profile that is most widely used is the Voigt profile. This function is a convolution of the simpler Gaussian and Lorentzian lineshape profiles. These two profiles each take into consideration a different broadening mechanism. The Lorentzian profile accounts for the effects of collision broadening. Collision broadening occurs when the line profile widens due to collisions between molecules. The Gaussian profile takes

into consideration the effects of Doppler broadening. Doppler broadening is caused by the thermal motion of the molecule. For example, a molecule moving with velocity, v, has associated with it a shift in the frequency, ν, from linecenter, ν_o, given by $\nu = \nu_o + \nu_o \frac{v}{c}$. This shift changes the energy of the photon required for absorption. Since the energy of a photon is given by E=hν, the line center shifts by the amount $\nu_o \frac{v}{c}$. The Voigt line profile accounts for both Doppler and collision broadening and is therefore more accurate than either the Gaussian or Lorentzian lineshape functions alone [10].

Although the Voigt profile is a good approximation, there is a need for further improvement. One major difficulty with the Voigt profile is that it inherently assumes that molecular collisions occur instantaneously. It then follows that the profile does not accurately estimate the contribution of the transitions in the region far removed from line center, i.e. in the wings. The Voigt profile also assumes hard collisions between molecules.

There are three other lineshape profiles that are more accurate than the Voigt profile. The Galatry profile, unlike the Voigt, assumes soft collisions between molecules. The function assumes that it takes many such collisions to alter the velocity of the molecule, whereas in the Voigt profile, only one collision is assumed to be sufficient to change the molecule's velocity. The Rautian and Sobelman profile is also different from the others. It assumes a hard collision as the Voigt, but does not assume an instantaneous collision [6]. The Berman speed-dependent Voigt profile was also found to be more accurate than the Voigt. This function differs from the Voigt in that it introduces a velocity dependence on the collisional broadening process. For all three functions

mentioned, the resulting profile is no longer a convolution of the Lorentzian and Gaussian profiles, as it is in the Voigt profile.

The importance of obtaining an accurate description of the lineshape function is clearly illustrated in the results of Ritter and Wilkerson [6] shown in Figure 2. This figure shows an observed profile and the results of

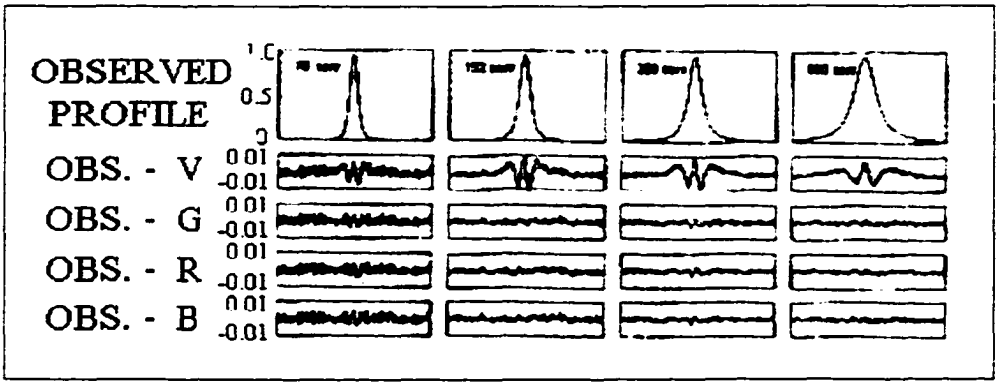

Figure 2 Observed absorption line profile and the differences between it and theoretical lineshape profiles. Voigt (V), Galatry, Rautain and Sobelman, (B) Berman [6].

the observed profile minus a theoretical lineshape function. Four lineshapes were used, the Voigt (V), Galatry (G), Rautain and Sobelman (R), and Berman (B). The later three all have significant improvement over the Voigt profile; hence we use the Rautain and Sobelman function in our calculations.

2.3 Absorption Lineshape Characteristics and Measurements

Measurements of absorption lines yield a lot of information about the sample gas. This information includes specie type, density, temperature, and velocity. These four measurements are explained in this section.

Each molecule has a unique absorption spectrum, and once a linecenter, ν_o, is determined for a measured absorption line then the molecule can be identified by matching it to known spectra of materials. Therefore, it is possible to identify all gases in a medium

by measuring the absorption lines within that medium and then matching them up to known lines for substances suspected to be in that medium.

The density of a molecule within a sample can also be determined by using absorption spectroscopy. In wavelength modulation spectroscopy, the magnitude of an absorption line follows a distinct pattern that can be compared to measured values of absorption lines to determine concentration or density of the molecule [5]. It has been shown, that at low concentrations the signal magnitude increases linearly with pressure, but after a certain critical density, which varies with harmonic order, the signal magnitude begins to decrease due to pressure broadening of the signal [5]. This effect is shown in

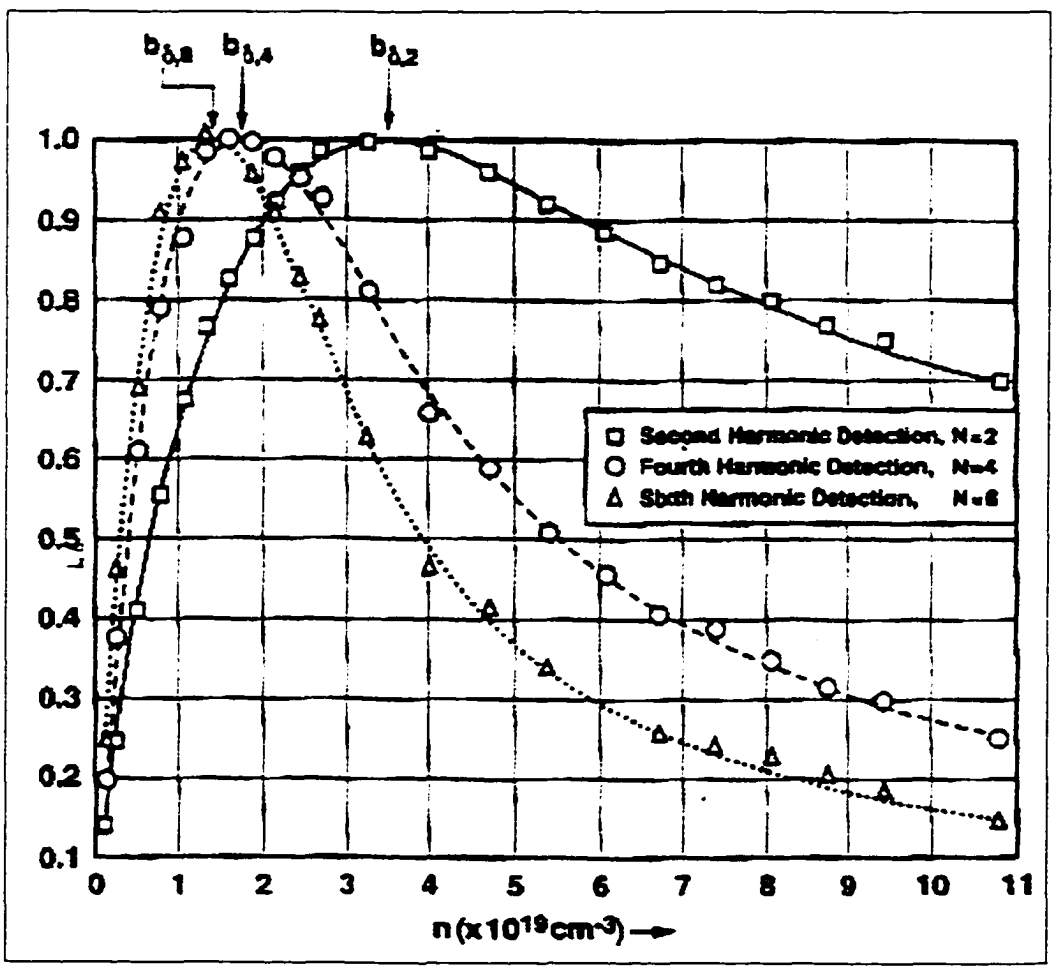

Figure 3 Signal Magnitude vs. Pressure for various harmonic detection orders [3].

Figure 3 [11]. By taking measurements at two different harmonic detection orders, it is possible to accurately determine the density of the molecule in the sample by comparing it to a curve similar to that shown in Figure 3.

The velocity of the sample can also be determined by studying absorption lines. The Doppler shift of line center can be used to determine the velocity of the molecule by making use of the equation: $\nu = \nu_o + \nu_o \frac{v}{c}$, where v is the velocity (along the line of sight) of the molecule, c is the speed of light in vacuum, and ν_o is the frequency at line center with v=0 [10].

It is also possible to determine the temperature of the sample from the lineshape function, by taking the ratio of two different lines. It can be shown that this ratio is proportional to exp(-ΔE/kT), where ΔE is the energy separation of the two line centers [11].

Higher harmonic detection wavelength modulation spectroscopy can also be used in the detection of overlapping lines. It has been shown that, by increasing the harmonic order, two overlapping lines that are indistinguishable at N=2 become resolved by N=6 [4]. Higher harmonic detection resolves these lines because the derivatives of the lineshape function magnify the deviation or distortion in the absorption profile caused by the interference of the overlapping lines. This allows an accurate interpretation of spectral regions even where these regions are congested. In addition, an accurate lineshape function helps in the resolution of overlapping lines by accurately modeling the entire profile including the wing structure, which can play quite an important role in the measured signal's profile.

This ability of resolving overlapping lines is shown in Figure 4. This figure displays the resolving power of higher harmonic detection by showing how two lines that combine to form what looks like a perfect signal for one line with second harmonic detection are resolved in fourth harmonic. At sixth harmonic, the distortion is even more dramatic, and information about the two lines can be extracted [4]. By being able to distinguish such lines, it may be possible to take several different types of molecules with close absorption lines, and monitor all of these molecules for temperature, velocity, and concentration simultaneously from one narrow scan of the spectrum [4].

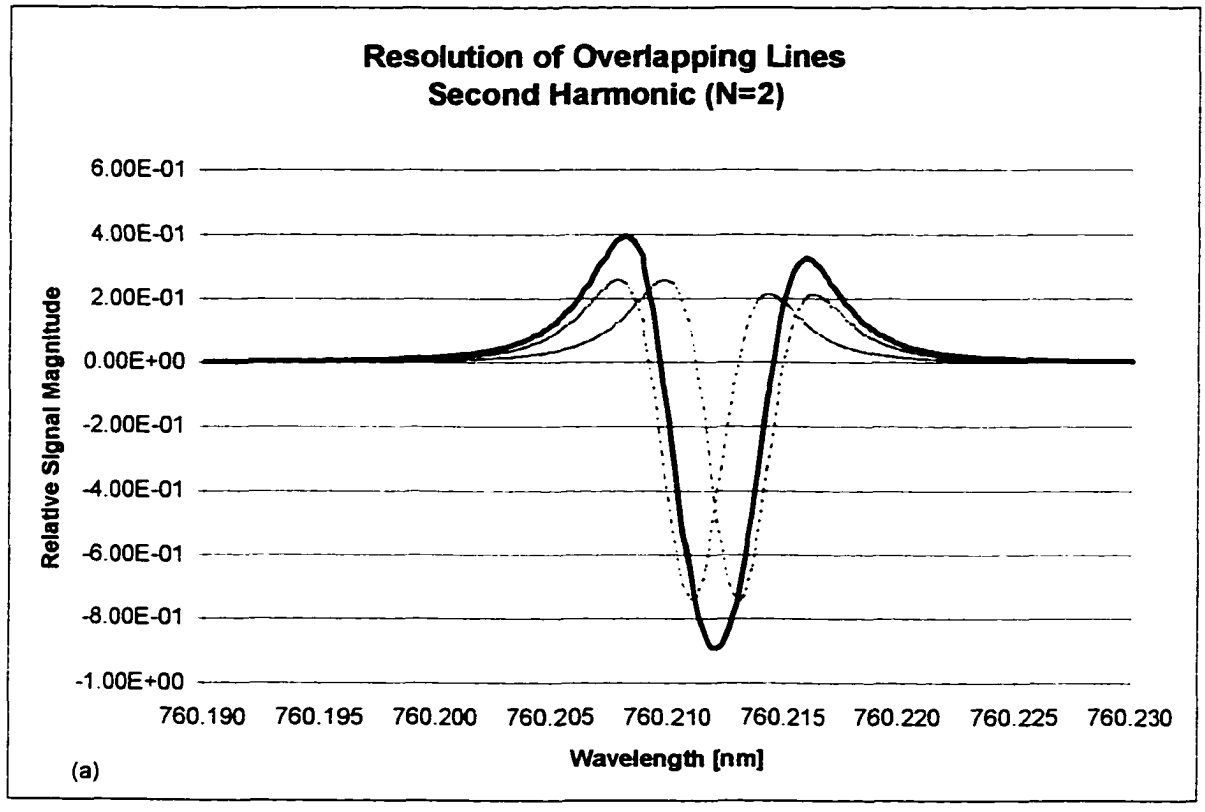

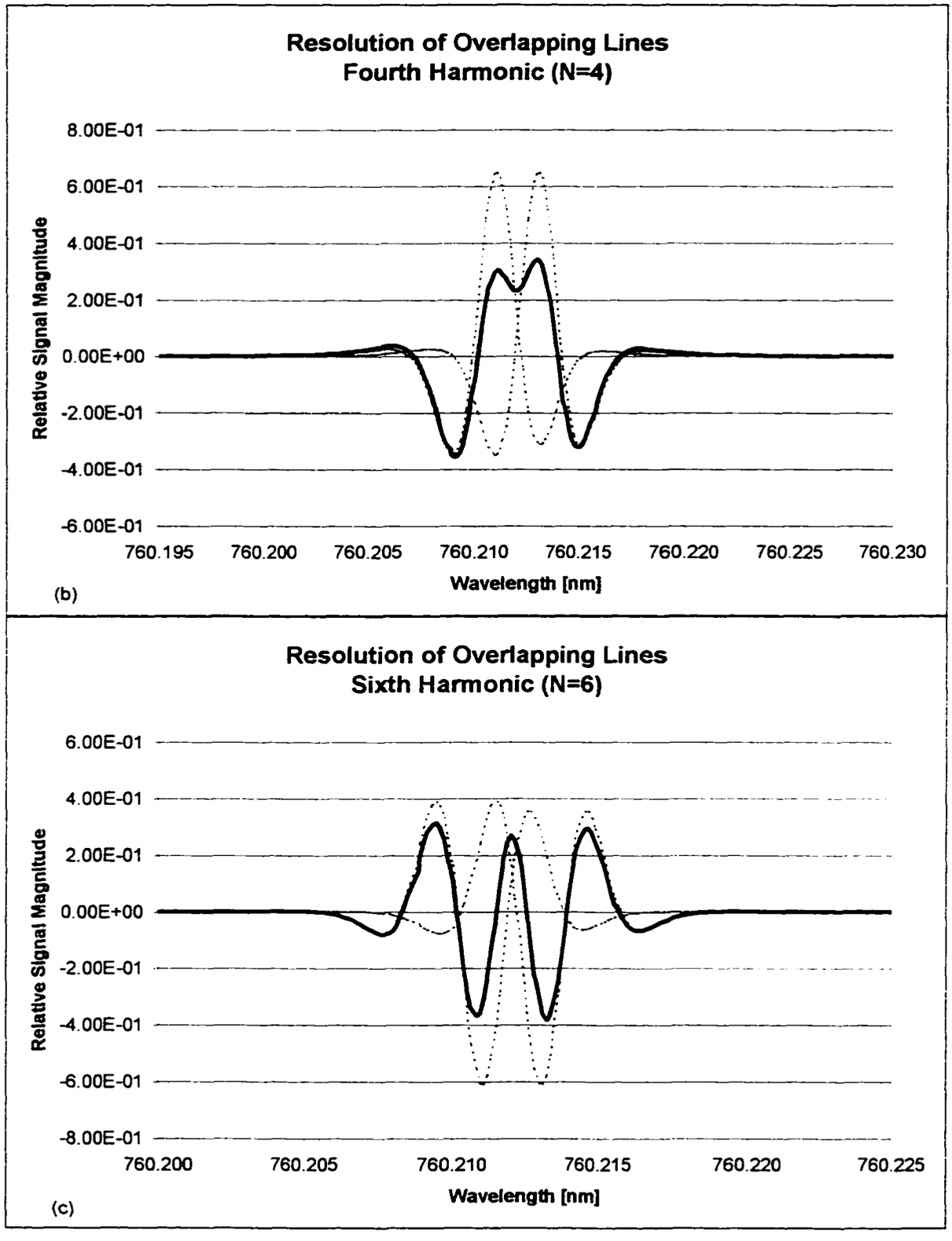

Figure 4(a-c) Calculated signals for typical overlapping lines. Dashed lines indicate individual lines; solid line indicates the sum of the two lines.

The measurements mentioned above can only be accurately made when there is an accurate lineshape function to compare them with. The task of determining an accurate lineshape function for use with a wavelength modulation spectroscopic experiment therefore becomes very important. This is seen in the resolution of overlapping lines where the wing structure plays an important role in the formation of the measured signal's profile. A lineshape function that accurately models the wing structure of the absorption profile is therefore vital for the interpretation of any data taken from such an experiment.

The understanding of molecular absorption and of the accurate forms of the lineshape profile are necessary conditions for characterizing absorption lines. Unfortunately, these are not sufficient conditions. One phenomenon that must be accounted for is Fabry-Perot fringing. Fabry-Perot fringing will be explained in detail in the next chapter, but, briefly, it is the distortion of a signal due to reflections off of parallel surfaces that are often unavoidable in optical experiments. It is important to note here that the fringing that occurs in an experiment distorts the signal and can make accurate modeling of the absorption line nearly impossible if it is not modeled and accounted for accurately. Details of the phenomenon of Fabry-Perot "etaloning," especially as it applies to wavelength modulation spectroscopy, are given in the following chapter.

CHAPTER III

FABRY-PEROT FRINGING IN WAVELENGTH MODULATION SPECTROSCOPY

The previous chapters have discussed the fundamentals of wavelength modulation spectroscopy. When conducting wavelength modulation spectroscopic experiments, one often notices a large periodic baseline noise signal imposed on the absorption signal. In order to eliminate this noise, it is common to try to re-align the optical equipment. Previous researchers have used two techniques to minimize fringing, explained in Chapter I. In this work, we show how etaloning can be minimized by higher harmonic detection. This is the first time that such a technique has been used [7].

During the course of wavelength modulation spectroscopy experiments, it was noticed that the noise was caused by one or more of the optical elements in the experiment, for example, the windows of the chamber containing the sample gas. By changing the position of the chamber, which effectively changed the input angle of the laser beam, it was possible to reduce the level of the fringing so that an absorption measurement could be made. Further study into the experiment allowed us to model the fringing. The modeling of this etaloning allows more accurate fits between theoretical and experimental results to be obtained.

3.1 The Fabry-Perot Etalon

The transmission function for the Fabry-Perot etalon is easily calculated by tracing the propagation of the electromagnetic wave through the etalon and calculating the output of each sequential pass of the reflected beam as leaves the resonating volume. As shown in Figure 5, the single input beam is modified by the etalon to form numerous output

waves. Each successive output wave has its own unique phase and magnitude. The phase shift between successive passes is determined by three parameters; the optical thickness of the etalon, the internal angle of incidence, and the wavelength of the laser beam. The magnitude of

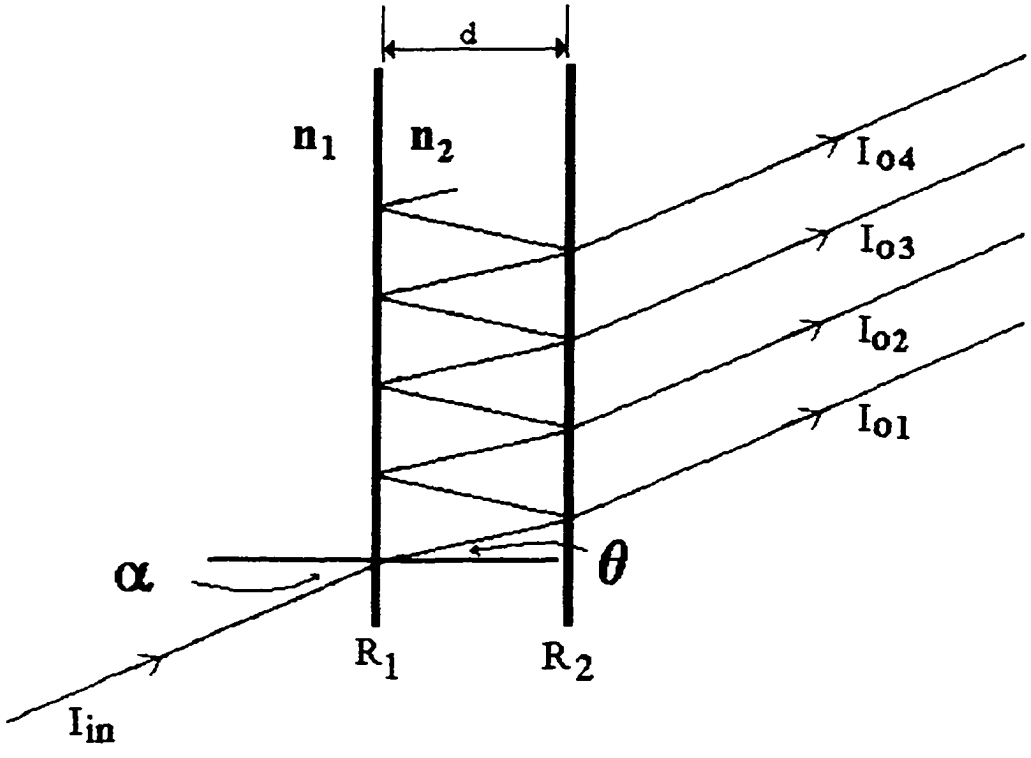

Figure 5 A Fabry-Perot Etalon showing the path of an EM wave incident upon the etalon.

each successive beam is equal to $R_2*R_1*I_{ox}$ where R_1 is the reflectivity of the first surface of the etalon, R_2 is the reflectivity of the second surface, and I_{ox} is the previous output intensity on the x^{th} pass, and $I_{o1}=T_1T_2$. A simple expression for the transmission of an electric field through the Fabry-Perot etalon can be written as [10]

$$E_T = E_o\left\{1 + \Gamma_1\Gamma_2 e^{-jk\cdot 2d} + \left(\Gamma_1\Gamma_2 e^{-jk\cdot 2d}\right)^2 + \cdots\right\}, \tag{3.1}$$

where Γ_1 and Γ_2 represent the reflectivity coefficients for the electric field for each of the two surfaces. The reflection coefficient is related to the reflectivity, R, by $R_{1,2} = |\Gamma_{1,2}|^2$ [10]. The transmission function for the Fabry-Perot etalon is then given by [12]

$$T_{FP} = \frac{I_{trans}}{I_{inc}} = \frac{(1-R_1)(1-R_2)}{\left(1-\sqrt{R_1R_2}\right)^2 + 4\sqrt{R_1R_2}\,Sin^2\left(\frac{\delta}{2}\right)}. \tag{3.2}$$

For our work, $R_1 = R_2 = R$ and by letting $\rho = \frac{4R}{(1-R)^2}$, the above expression reduces to

$$T_{FP} = \frac{I_{trans}}{I_{inc}} = \frac{1}{1+\rho Sin^2\left(\frac{\delta}{2}\right)}, \tag{3.3}$$

where $\delta = \frac{4\pi nd\cos(\theta)}{\lambda}$, and θ is the internal angle of reflection as shown in Figure 5 [12]. The transmission function is dependent upon the material's index of refraction, the reflectivity of the surfaces, the length of the etalon, the input angle of the laser beam, and the frequency or wavelength of the light passing through the etalon.

To show these effects, calculations were made for a reference set of values, and then the calculations were performed by changing only one parameter at a time to show its effect on the fringe pattern. The parameters of interest are the etalon's thickness, d, index of refraction, n_2, and the input angle, α, of the incident light. As seen in Figure 6, the etalon thickness and input angle only changed the etalon's free spectral range (FSR). This follows because as can be seen from Equation 3.3, the free spectral range is [10],

$$FSR = \frac{c}{2nd\cos\theta}. \tag{3.4}$$

The magnitude of the transmission function is primarily a function of the reflectivity, which itself is a function of the index of refraction of the material. The reflectivity is given by $R = \left(\frac{n-1}{n+1}\right)^2$. Therefore a change in the index of refraction causes

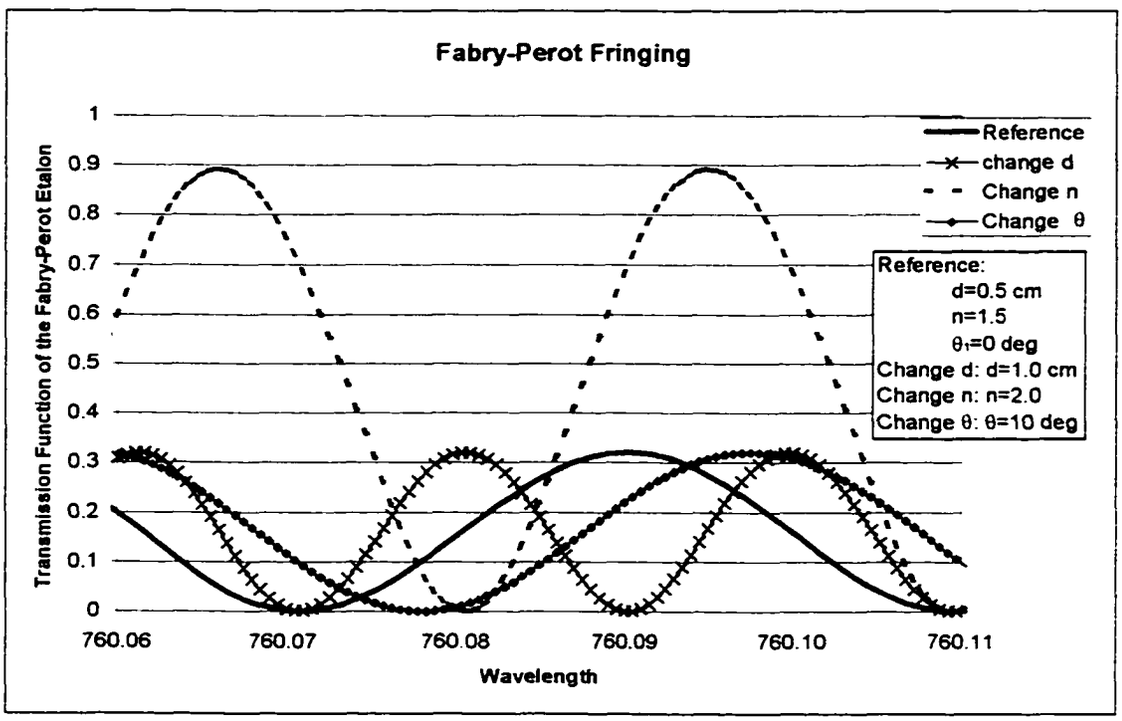

Figure 6 Calculated Fabry-Perot fringing to show the effects of d, n, and theta.

a change in both the magnitude and the period of the fringe. It is seen that even relatively small changes in the etalon's parameters change the etalon's transmission function sufficiently to cause a relatively large change in an absorption line profile and magnitude. Details of this effect are given in Section 3.3 below.

3.2 A Simple Model Incorporating Fringing in Wavelength Modulation Spectroscopy

The total transmission function for the absorption was assumed to be a product of the Fabry-Perot transmission function and the molecular absorption line transmission function. Hence,

$$T_{total} = T_{abs} T_{FP} \tag{3.5}$$

The transmission function for the absorption line in its simplest form can be expressed as [10]

$$T_{abs} = \exp(-n\sigma l), \tag{3.6}$$

where n is the density of absorbing molecules in units of cm^{-3}, σ is the absorption cross section in cm^2, and l is the path length in cm. The two expressions for the transmission functions in Equations (3.3) and (3.6) can be combined to form

$$T_{total} = \exp(-n\sigma_{total} l) = \exp(-n\sigma_{abs} l) \frac{1}{1 + \rho \sin^2\left(\frac{\delta}{2}\right)}. \tag{3.7}$$

One may view Equation (3.7) as a definition of the total absorption cross-section, σ_{tot}, in a system with an absorption line and an etalon.

Using the definition $\sigma = \bar{\sigma} g(\nu)$, where $\bar{\sigma}$ is the integrated absorption cross-section, the above equation can be solved for $\overline{\sigma_{tot} g_{tot}}(\nu)$ to give the following expression

$$\overline{\sigma_{total} g_{total}}(\nu) = \overline{\sigma_{abs} g_{abs}}(\nu) + \frac{1}{nl} \ln\left[1 + \rho \sin^2\left(\frac{\delta}{2}\right)\right]. \tag{3.8}$$

Now, it has been shown that an appropriate equation for expressing a wavelength modulation absorption profile can be written as [11]

$$\frac{S^N}{I_o} = \frac{2^{1-N} \beta^N}{N!} nl \overline{\sigma_{abs}} g^N(\nu), \tag{3.9}$$

where β is the frequency modulation index and N is the harmonic detection order. This equation is only valid for small frequency modulation indices, and it assumes that there is no amplitude modulation. g^N is the N^{th} derivative (with respect to frequency) of the lineshape function g(ν). If, $\overline{\sigma_{abs}}g(\nu)$ in Equation (3.9) is replaced by $\overline{\sigma_{tot}}g(\nu)$ given in Equation (3.8), then the equation for the absorption signal, including the Fabry-Perot etalon, becomes

$$\frac{S^N}{I_o} = \frac{2^{1-N}\beta^N}{N!}\left(nl\overline{\sigma_{abs}}g_{abs}(\nu) + \sum_M \ln\left[1+\rho\sin^2\left(\frac{\delta_M}{2}\right)\right]\right), \tag{3.10}$$

where M is the integer number of passes the laser beam makes through the etalon. $\delta_M = \frac{4\pi nd\cos(\theta_M)}{\lambda}$, where θ_M is the internal angle of incidence for each pass. In a typical experiment there are two etalons, one at the front of the absorption chamber, and one at the end of the chamber.

To test this equation a Lorentzian lineshape profile was initially assumed for g(ν). The Lorentzian was chosen because it is mathematically simple, and its derivative is easily calculated. The derivative representation for the absorption profile was chosen because it is yields a simple and easy-to-follow formulation for higher harmonic detection orders. The equations were programmed into Mathematica. Mathematica is a sophisticated mathematical software package that can accurately calculate and plot the derivatives of complex functions including our expression for the wavelength modulation signal given above in Equation (3.10).

Theoretical Results, First Harmonic Detection (N=1)

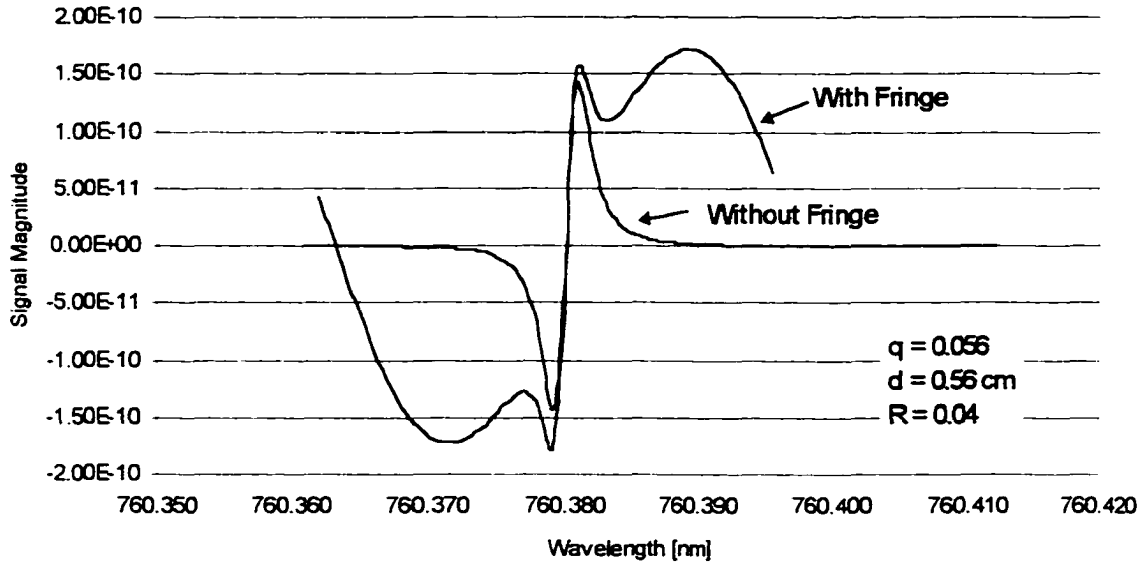

Theoretical Results, Second Harmonic Detection (N = 2)

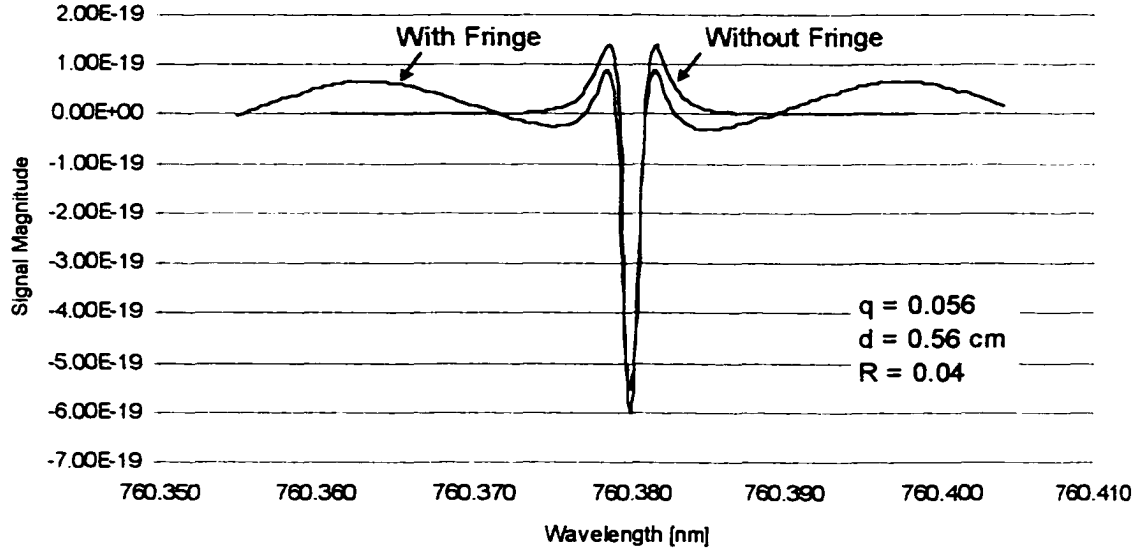

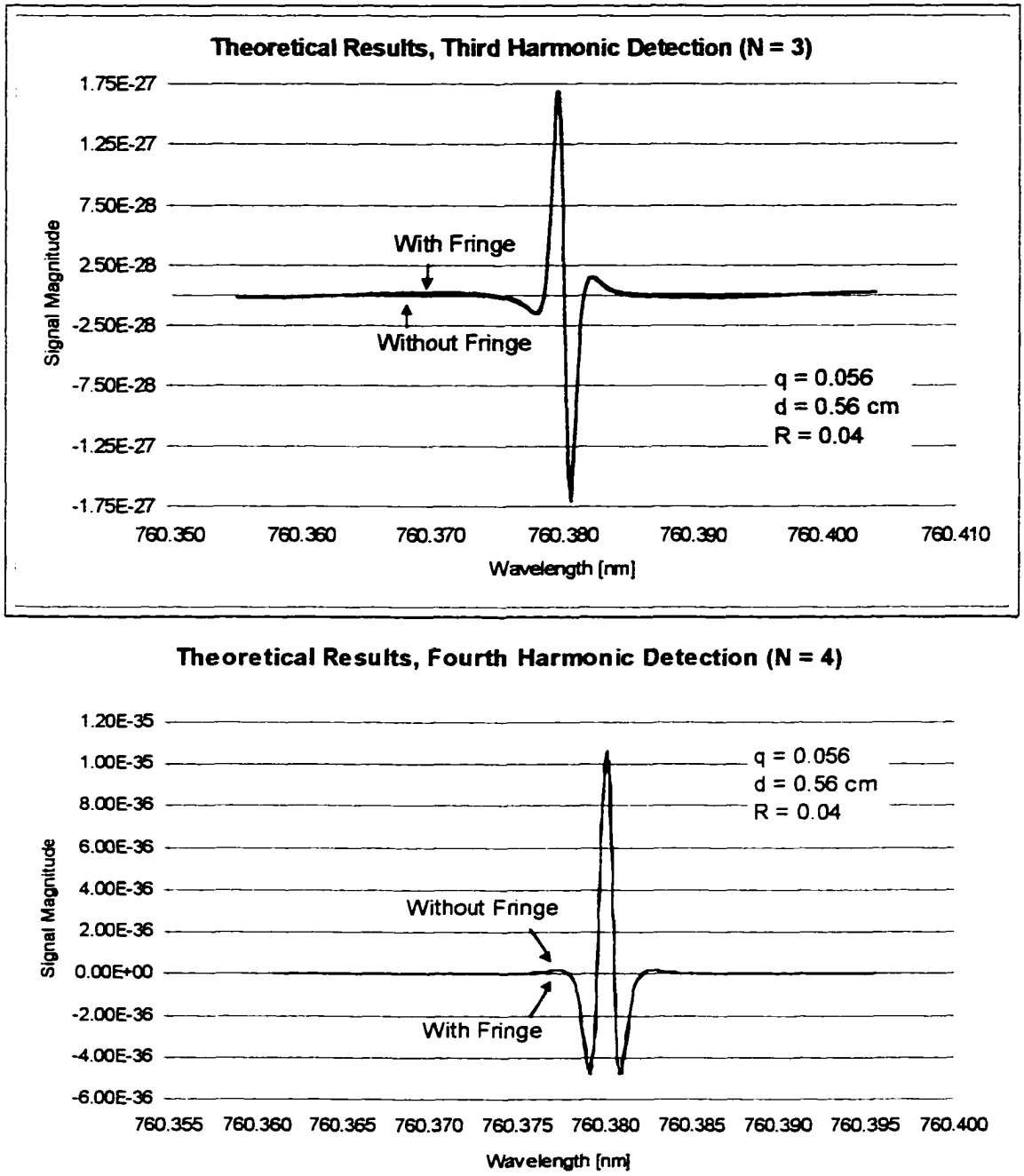

Figure 7(a-d) Approximate theoretical results using the simple theory showing an absorption line with and without fringing.

The initial results from the approximate theory, shown in Figure 7(a-d) above, were promising; however, it is well-known that Equation 3.9 can, at best, only yield qualitative agreement with experimental data, since it does not account for either the finite

magnitude of the frequency modulation index nor the presence of residual amplitude modulation. Furthermore, a Lorentzian lineshape function is only an approximation. It therefore is necessary to refine the model further. This was done by incorporating the Rautian-Sobelman lineshape function, which has been shown to be more accurate than even the Voigt profile (and certainly much more applicable than the simple Lorentzian used in Figure 7 above) [6]. In addition, the effects of finite wavelength and amplitude modulation indices were included. Details of these refinements, needed to accurately model etaloning effects in a wavelength modulation experiment, are given next.

3.3 A Detailed Theory Incorporating Fringing in a Wavelength Modulation Spectroscopy Experiment

In order to properly model the fringing effects caused by a Fabry-Perot etalon introduced by optical components, it is necessary to use an expression that includes the effects of modulation (amplitude and frequency) broadening [11], as well as pressure broadening. There is currently a program written by Audra Bullock that performs such a calculation. The program uses Wilson's method for calculating wavelength modulation spectroscopy signals [13]. The program was modified to include equations for calculating the fringing components of the signal. This was done by using Equation 3.7 above for σ_{total}.

The results of calculations using the complete theory are shown in Figure 8. These results were obtained by using experimental values for both the absorption line and the fringing. The values for the absorption line were taken from HITRAN '96 for the line RR(15,15) in the oxygen A-band. The values for the Fabry-Perot fringing are d=0.5 cm, n=1.5, which implies R=4%, and $\theta=0^{\circ}$. It was also assumed that there were two passes

through the Fabry-Perot etalon. These values are consistent for a chamber having glass windows with thickness equal to 0.5 cm.

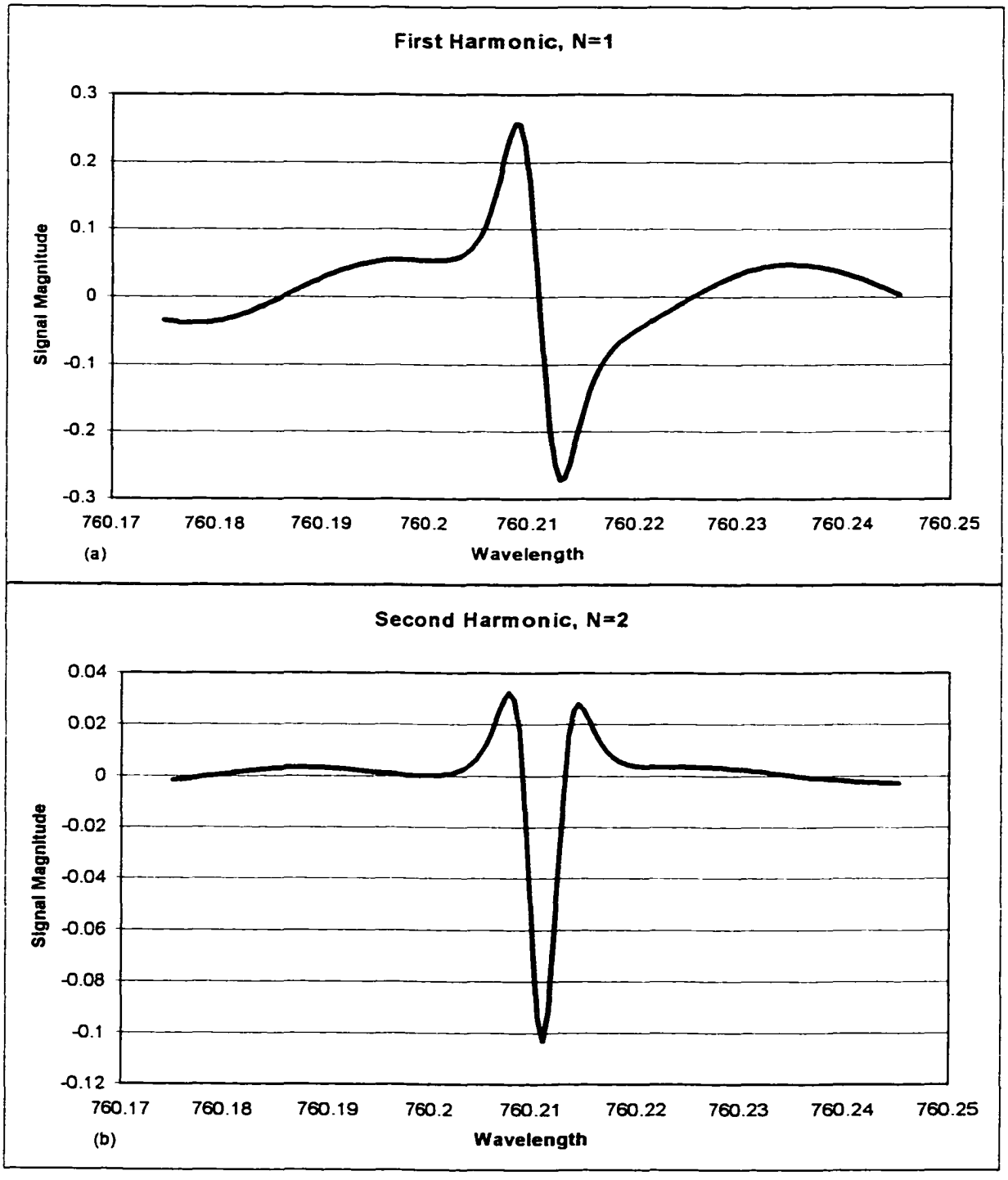

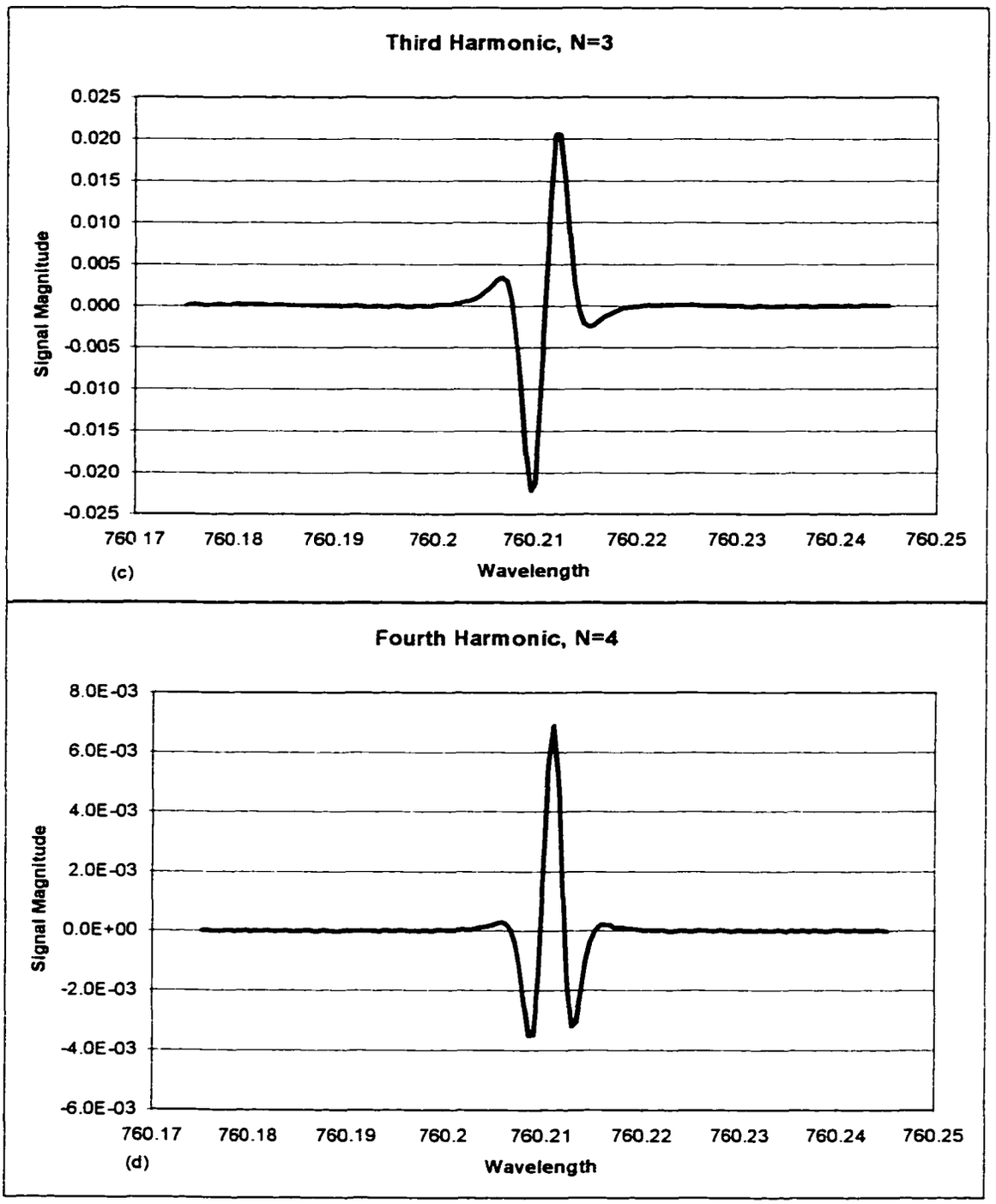

Figure 8(a-d) Calculated signal, including Fabry-Perot fringing, using the complete theory, HITRAN Database values for the absorption line (RR(15,15)), and realistic values for the etalon parameters.

As seen in Figure 8(a-d), the fringing does not reduce as quickly as in the approximate results in the previous section. In Chapter IV, these theoretical results are compared with experimentally obtained data. The results seen there show excellent

agreement between theory and experiment. It is important to notice in these results that although there is a large component due to fringing in the first harmonic signal, and even residual fringing in second harmonic, there are no apparent contributions in third or fourth harmonics. This result is actually a general one for situations when the quality factor of the etalon is smaller than that of the absorption line (this is discussed in detail in Section 3.5. *The ratio of the signal compared to the fringe, which we have termed signal to fringing noise ratio (SFNR), increases with harmonic detection order.*

The results obtained from these calculations were found to accurately model both the absorption line and the fringe with a high degree of accuracy. It was found that the fringing is highly dependent upon the etalon's parameters, and that even the slightest change in any of the parameters has a dramatic effect on the signal. This property tends to make matching experimental data very difficult, but with an understanding of how the parameters influence the results, matching becomes possible.

The theoretical outline given in Section 3.5 below shows under what circumstances one may expect an increase in signal to fringing noise ratio with increasing harmonic detection order.

3.4 Increase in SFNR with Harmonic Order

The emphasis of the work included in this chapter is in improving the overall quality of the experiments conducted in the laboratory. What started as a way to improve experimental signal to noise ratios by realigning the optical equipment evolved into a comprehensive study and modeling of Fabry-Perot fringing. While first proposing the concept of Fabry-Perot fringing, we predicted that under some circumstances the SFNR

should increase with harmonic detection order. After conducting some initial calculations, this was confirmed in laboratory experiments discussed in Chapter IV.

In an attempt to predict the increase in the SFNR, a study of the ratio of the quality factors for the absorption line and the etalon was conducted. The equations for the quality factor for both the absorption line and the Fabry-Perot etalon are well known and are given in Equations (3.10) and (3.11).

$$Q_{Line} = \frac{\nu_o}{\Delta\nu_{12}} = \frac{\lambda_o}{\Delta\lambda_{12}} \qquad [10] \quad (3.10)$$

$$Q_{FP} = \frac{2\pi nd\cos(\theta)\sqrt{R}}{\lambda_{oFP}(1-R)} \qquad [12] \quad (3.11)$$

We define q as the ratio of the quality factor for the Fabry-Perot etalon to the quality factor for the absorption line.

$$q = \frac{Q_{FP}}{Q_{Line}} = \frac{m\pi\sqrt{R}}{(1-R)Q_{Line}}, \qquad (3.12)$$

where $$m = \text{IntegerPart}\left[\frac{2nd\cos(\theta)}{\lambda_{oLine}}\right] \qquad (3.13)$$

The integer m is the peak in the Fabry-Perot transmission function immediately to the lower wavelength side of the absorption line. The integer m is representative of λ_{oFP}.

The next set of figures, obtained by using the full theory described in Section 3.4 above, show how the SFNR varies with q. The graphs also show how the SFNR increases with harmonic order, and how that increase depends on q.

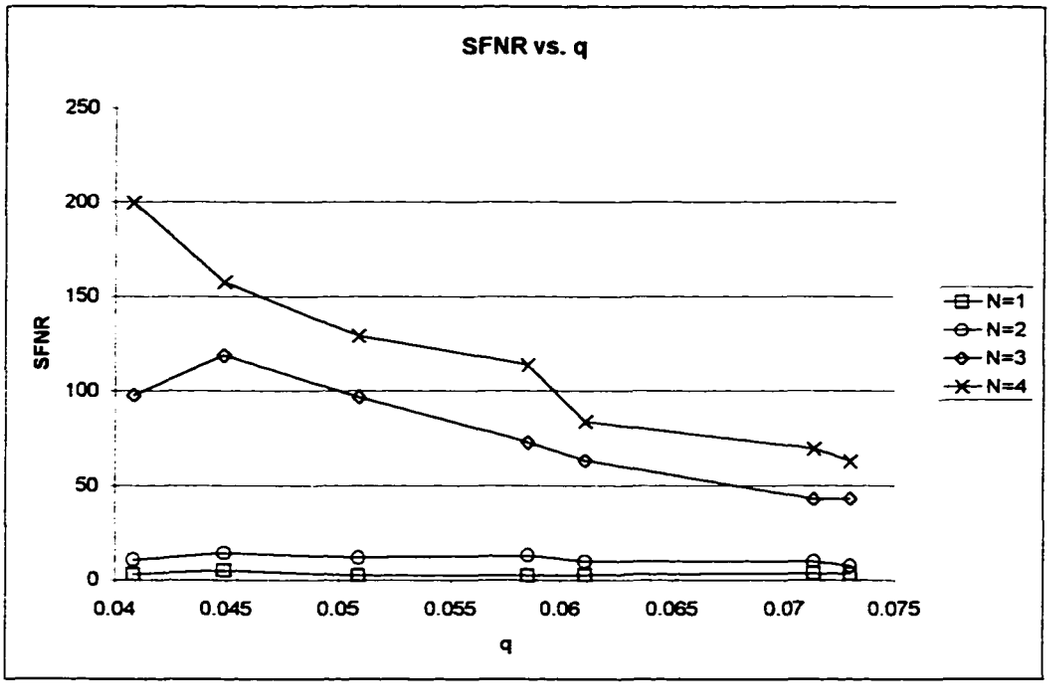

Figure 9 Calculated SFNRs vs. q for harmonics detection orders 1 through 4. Lines are for visualizing the variation of the SFNR only. The data is discrete in nature.

Figure 9 shows the relationship between SFNR and q for a given harmonic detection order. The graph shows how the SFNR decreases with increasing q. This implies that as the quality factor of the etalon is increased, the signal quality deteriorates. Although only a small range of q is shown here, the effect is consistent for all values of q. Calculations were done for a much larger range of q using the approximate theory and showed the analogous results. The approximate results are slightly inaccurate due to the approximations, and therefore those results are not shown here. The results in Figure 9 were calculated with the complete theory and are representative of experimentally observed values for q, where Plexiglas, glass, or a similar material is used for optical windows. It is important to notice that in fourth harmonic, the SFNR varies from 60 to 200. This large difference shows the importance of modeling the fringe so that the source of fringe can be identified and the fringing be minimized.

Figure 10, below, shows the signal to fringing noise ratio vs. harmonic detection order with a variation in the index of refraction of the material while all other parameters are held constant. The index of refraction influences both the magnitude of the fringe and

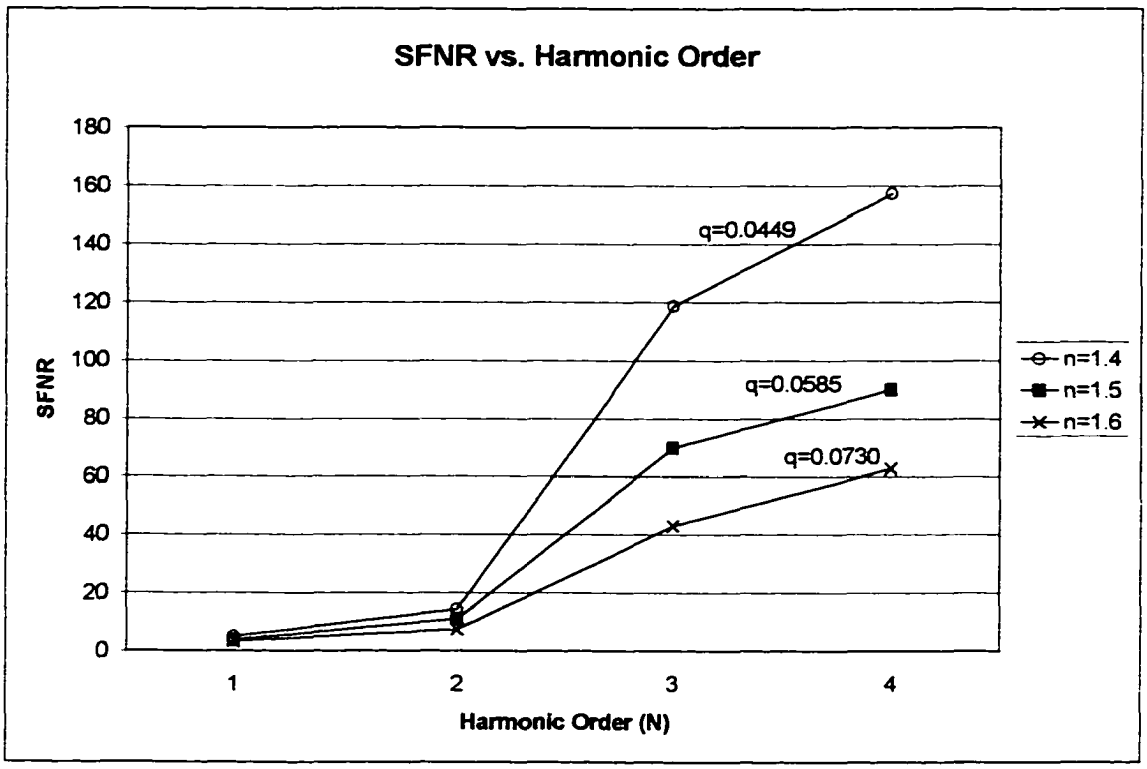

Figure 10 Calculated SFNR vs. Harmonic Order with changes in the index of refraction of the etalon. Lines are for visualizing the variation of the SFNR only. The data is discrete in nature.

the FSR. The variation in the index of refraction was used to vary the ratio of the quality factor of the etaloning element to that of the absorption line, q. The larger magnitude of the fringe primarily affects the lower harmonics (N = 1, 2). By N=3, the derivative like property of harmonic detection shifts the emphasis on the slopes of the previous harmonic, and therefore the SFNR is fairly large for the higher harmonics.

Figure 11, is similar to Figure 10 except that the parameter d (the etalon length) was varied instead of the index of refraction, n. The smaller the value of q, the larger the increase in SFNR.

This type of analysis can be used to predict how an experiment might turn out, or more importantly, which harmonic detection orders can be used to obtain acceptable data. For example, if a third order detection experiment was to be performed, and a SNR of 50 was required, then a q less than 0.0713 is needed if there is no other noise source in the system.

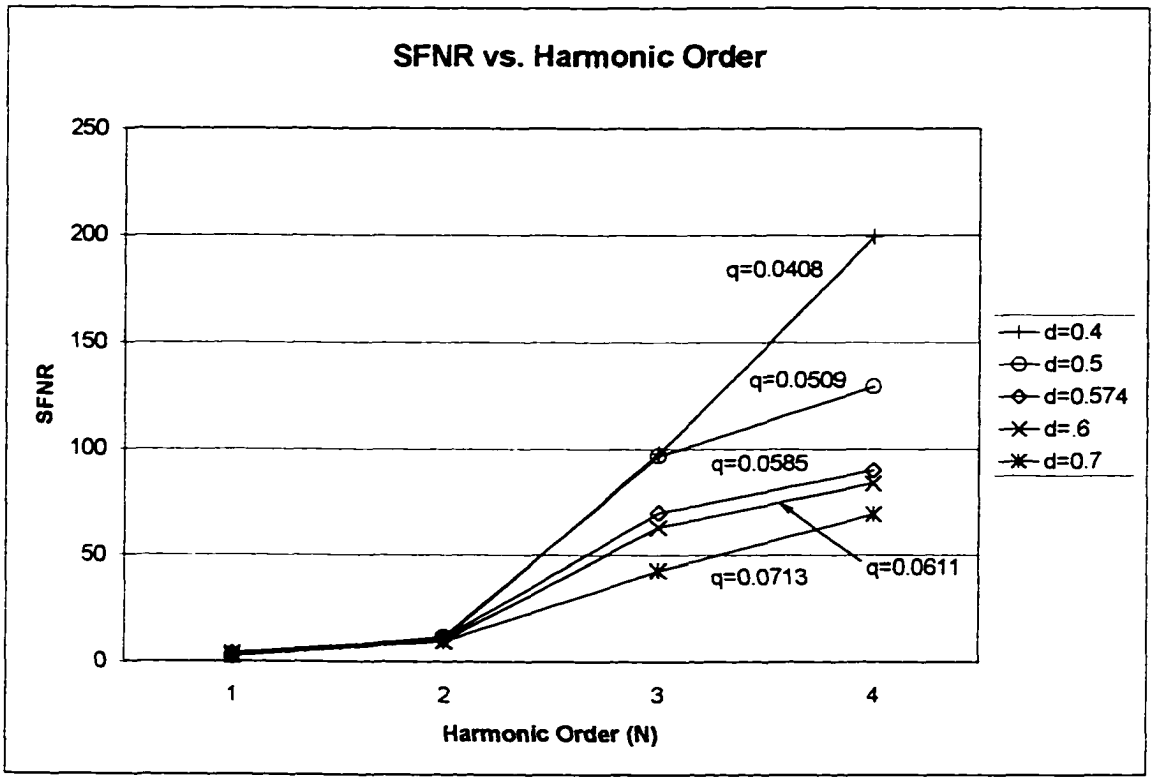

Figure 11 SFNR vs. Harmonic Order with changes in the length of the Fabry-Perot etalon. Lines are for visualizing the variation of the SFNR only. The data is discrete in nature.

Figure 12 shows SFNR vs. harmonic detection order with a variation in the angle of incidence of the laser beam. The angle α shown in Figure 5 is the external angle of incidence, which relates to θ in the Fabry-Perot equations by the relation $\theta = \sin^{-1}\left(\frac{n_1}{n_2}\sin\alpha\right)$. As seen in the graph, small changes in θ do not change the value of q very much, and hence, the SFNR curves are all about equal. The variations are caused

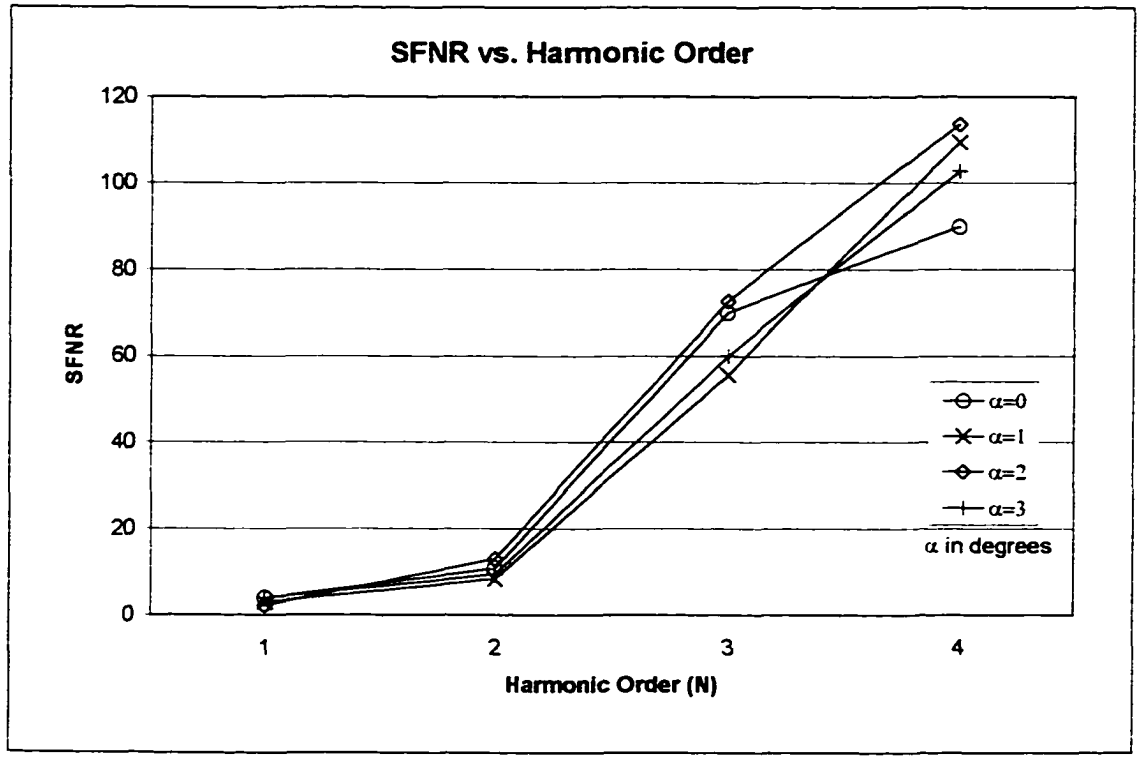

Figure 12 SFNR vs. Harmonic Order with a change in θ from 0 to 3 degrees. The other parameters are the same as those in Figure 10 and 11. Lines are for visualizing the increase in the SFNR only. The data is discrete in nature.

more by how the line overlaps with a peak in the Fabry-Perot transmission function. If the peak of the Fabry-Perot's transmission function directly overlaps linecenter for the absorption line, than the effects of fringing are less than for the same etalon used in conjunction with an absorption line that lies in the interval between a peak and trough.

CHAPTER IV

EXPERIMENTAL INVESTIGATION OF ETALONING IN WAVELENGTH MODULATION SPECTROSCOPY

The results of experiments done to investigate the effects of etaloning in wavelength modulation spectroscopy experiments are described in this chapter. A comparison of these experimental results to the theoretical model developed in Chapter III is given, and good agreement is obtained. The results discussed in this chapter are also described in a recent journal article [7].

4.1 Experimental Procedure

A series of wavelength modulation experiments were performed. Wavelength modulation experiments using a diode laser are conducted by the following procedure. A slow ramp is fed to the diode laser with a DC bias current approximately equal to the threshold lasing current. An AC current is injected in addition to the ramp. In our case, the AC modulation frequency is between 8 and 10 kHz. The modulation frequency is used to shift the signal to a region with relatively little noise [3]. Phase sensitive detection is performed using a Lock-in amplifier, which can be set to detect a signal at a particular harmonic of the modulation frequency [3]. The PC was equipped with a data acquisition card (DAQ) for reading the voltage across a resistor that was connected in series with the diode laser. This allows the AC and DC current through the diode to be measured. The computer also has a general purpose interface bus (GBIB) for communicating with the Lock-in amplifier and the wavemeter so that the data can be read simultaneously and recorded with a time stamp to increase the accuracy of the data collection system.

The experimental apparatus and layout is shown in Figure 13. The multipass cell can be set up to have any even number of passes depending on the separation of the two mirrors. For the experiment in sections 4.2 (a.1-3), the mirrors were separated by 68 cm

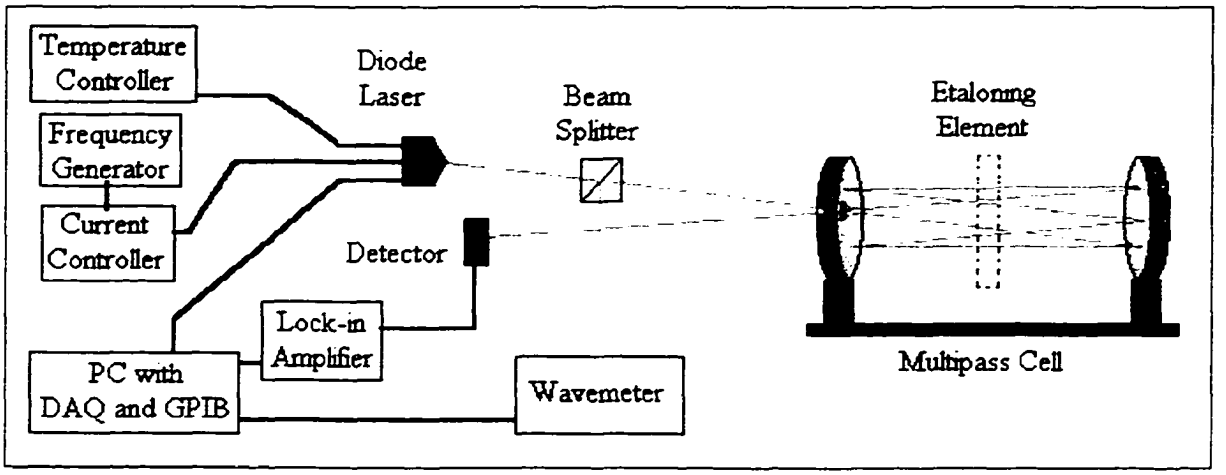

Figure 13 Experimental Layout for a wavelength modulation experiment.

to allow for ten passes. The multipass cell makes measurements in air, and therefore has no chamber windows to introduce etaloning. This is advantageous in that it allows for a baseline measurement to be made without fringing and theoretical matching of the line can then be done accurately. A Plexiglas blank was then inserted into the multipass cell so that there were effectively the same number of Fabry-Perot etalons as there are passes in the cell.

4.2 Experimental Results

Results of experiments performed with the multipass cell with and without the controllable fringe introduced by the Plexiglas blank are presented in this section. Experiments were conducted with an optical blank inside the multipass cell as well as without the blank. The experiments with the blank inside the cell introduced controllable fringes. In these experiments, the orientation of the Plexiglas blank was altered to provide

a unique fringe pattern for each experiment that was used to test the validity of the equations developed to model Fabry-Perot fringing. The experiments without the blank yield a baseline result and a comparison between the experiments with and without the controllable fringe then gives the effects of etaloning. Theoretical results are computed using the full theory (which accounts for the nonzero values of the amplitude and frequency modulation, and also incorporates the phase difference between these two types of modulation) for all experiments.

4.2 (a) Experimental and Theoretical Results for the RR(15,15) Absorption Line Using a Ten Pass Multipass Cell

This section shows measurements of the absorption line RR(15,15), in the oxygen A-band, with and without fringing. The baseline measurement is relatively "clean" for an absorption measurement showing that there was negligible etaloning in the apparatus. As seen in Sections 4.2 (a.2-3), the measured signal can be distorted and difficult to both recognize and model if there is any significant etaloning. The results shown in Sections 4.2 (a.2-3) are those for which we introduced controllable fringing into the apparatus

4.2 (a.1) Baseline Measurement without an Etaloning Element

In order to demonstrate the effects of etaloning and theoretically model the fringing, one needs to have a baseline result. This was obtained by making measurements without the Plexiglas blank inside the multipass cell.

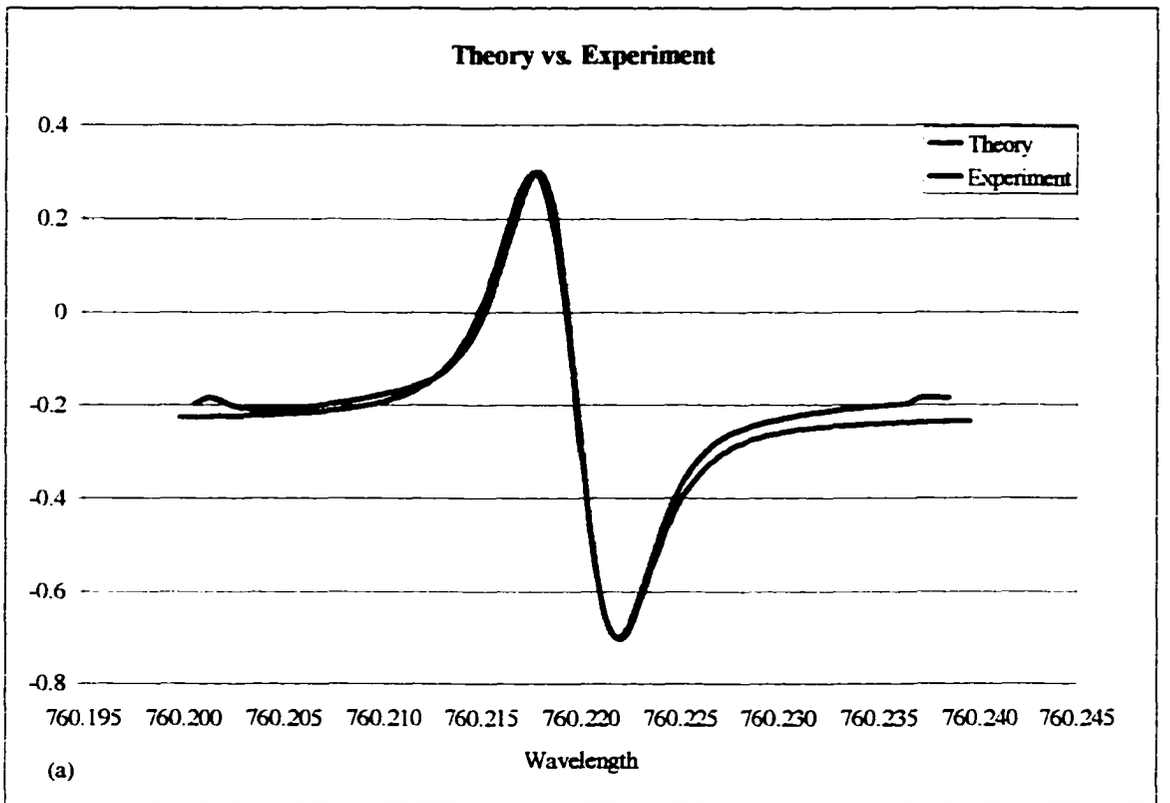

(a)

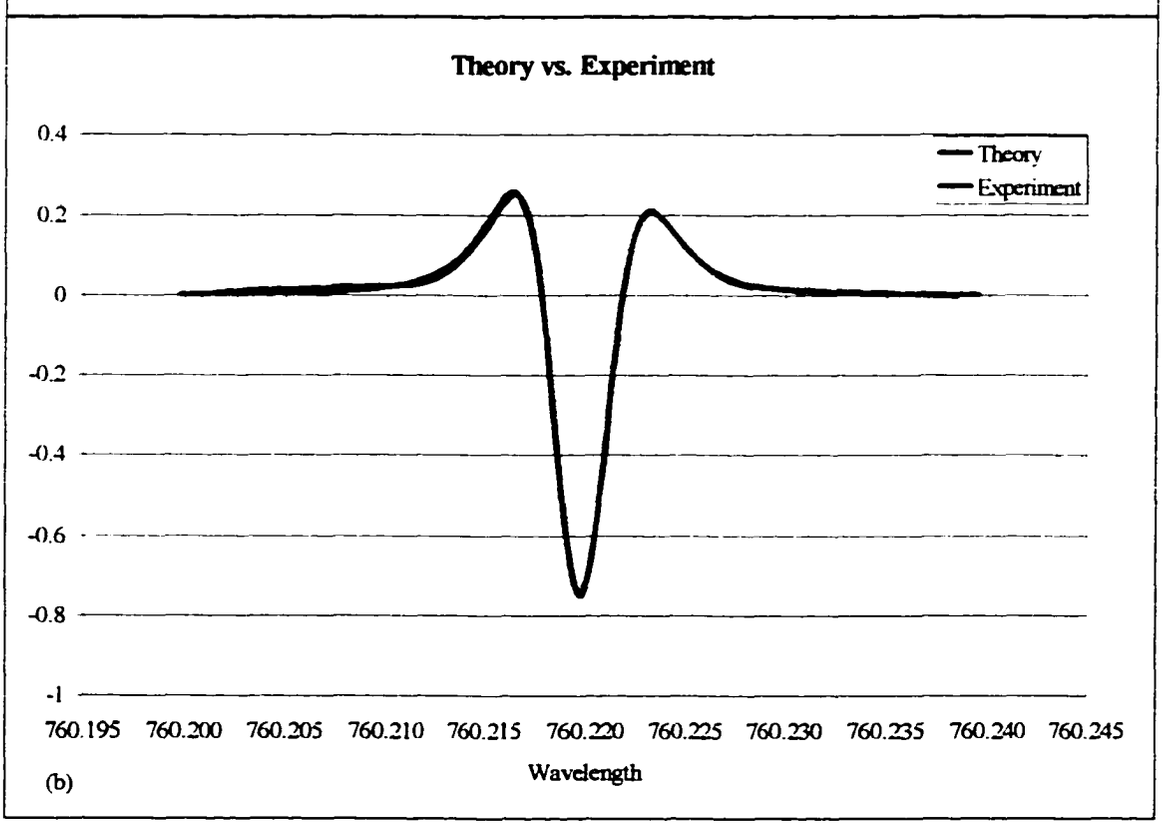

(b)

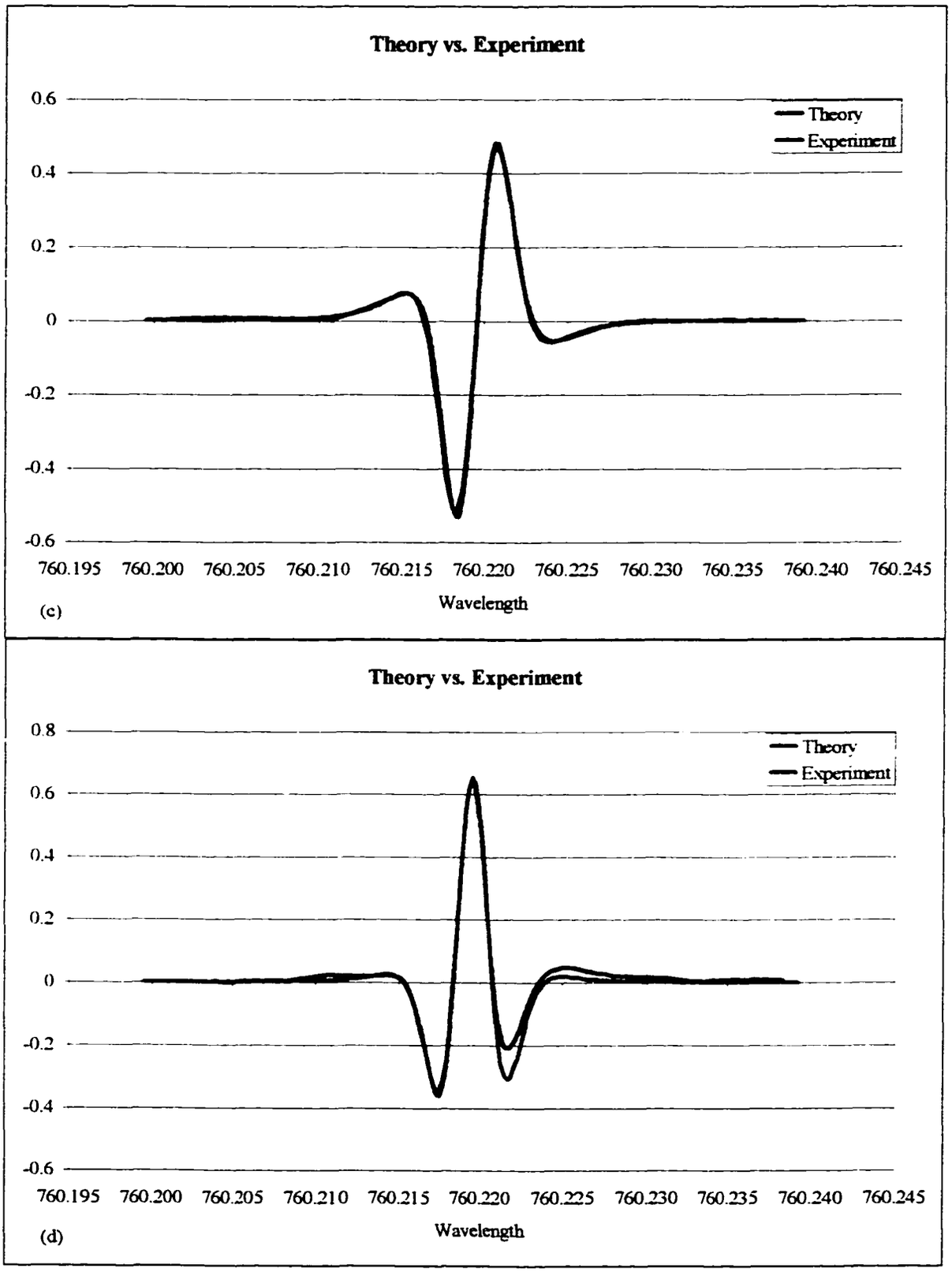

Figure 14(a-d) Experimental and theoretical results for harmonic detection signals, N=1-4, for the RR(15,15) line without fringing (Baseline measurement).

Figures 14(a-d) show the experimental results obtained for the wavelength modulation spectroscopic absorption measurement performed using first through fourth harmonic detection respectively. While several different lines have been measured, Figure 14 shows the results for the oxygen RR(15,15) A-band line. The figure also shows computed signals. The latter were obtained by using the Rautain Sobelman lineshape profile. The theoretical calculation technique has been outlined in detail in References [6, 11, 13]. The calculations used the values of experimentally measured modulation indices. The values for linecenter and line widths that gave these theoretical results were 760.202 nm for linecenter and 0.043 cm^{-1} for line width. The theoretical curves were calculated using a Rautian-Sobelman profile and match the experimental curves very well. A noticeable discrepancy between the theoretical and experimental results occurs in fourth harmonic. This error is probably due to under-modulation. (The latter occurs when the signal - fourth harmonic signal in this case - is so small that one obtains discretization errors in the digital signal processing performed by the lock-in amplifier.)

4.2 (a.2) Intracavity Etaloning Element Normal to the Optic Axis

In Figures 14(a-d), the absorption signal is easily recognized and matched with theoretical profile. Figure 15 shows the results of experiments performed with the blank inside the multipass cell. The Plexiglas blank was inserted into the center of the multipass cell perpendicular to the normal of the mirrors. The blank had a thickness of 0.574 cm. and an index of refraction of 1.5. The ten angles made by the beam as it traveled through the blank in the ten-pass cell were obtained by measuring the locations of intersection between the mirror surface and the laser beam. These angles where obtained by using the equation of a line in three-dimensional space, and by taking the dot product with the

normal vector for the blank. The ten angles were found to be 2.6, 2.6, 2.9, 3.3, 3.3, 3.4, 3.5, 3.6, 3.7, and 3.7 measured in degrees. These angles were varied by no more that two percent from these values to obtain the fits shown. The variation (in the calculations) in the angles of two percent from measured values is valid because the estimated maximum experimental error in the measurement of these angles is also approximately two percent. The parameters that were used to model the absorption line are the same those used for modeling the signal without fringing.

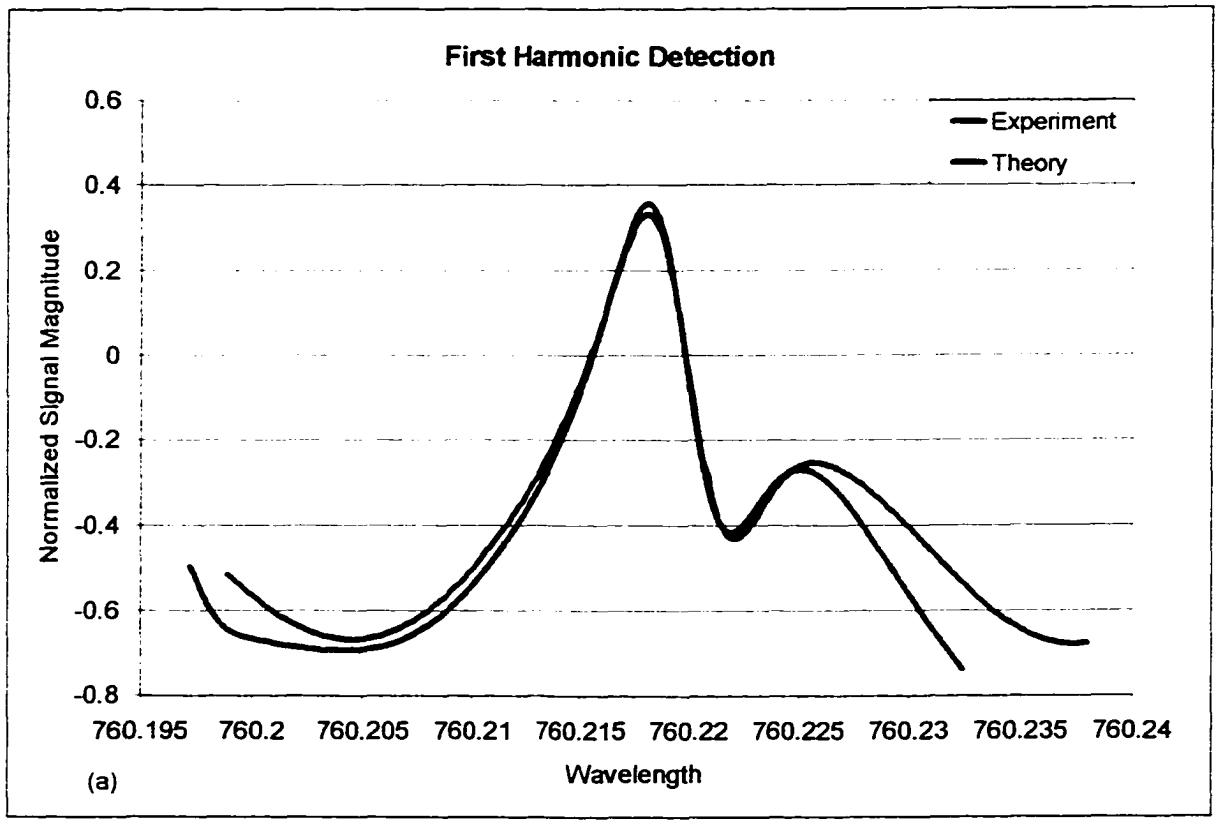

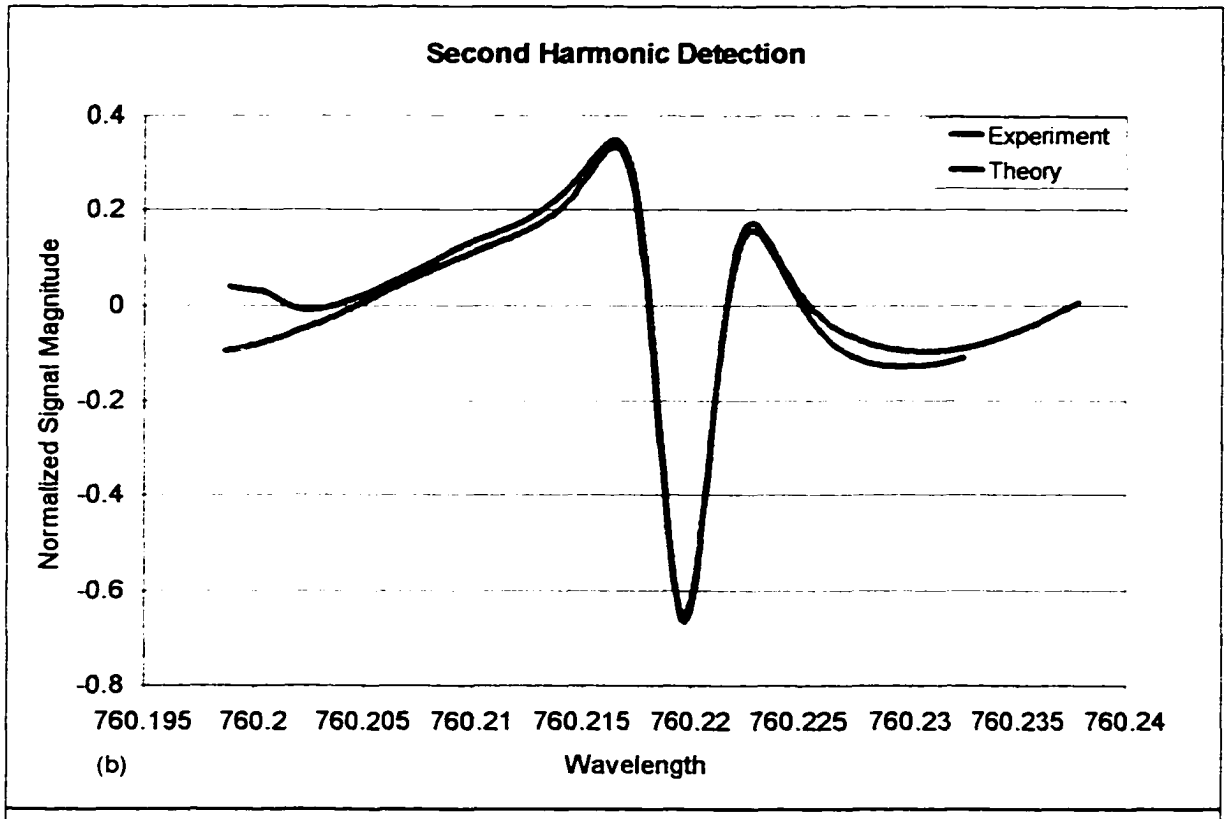

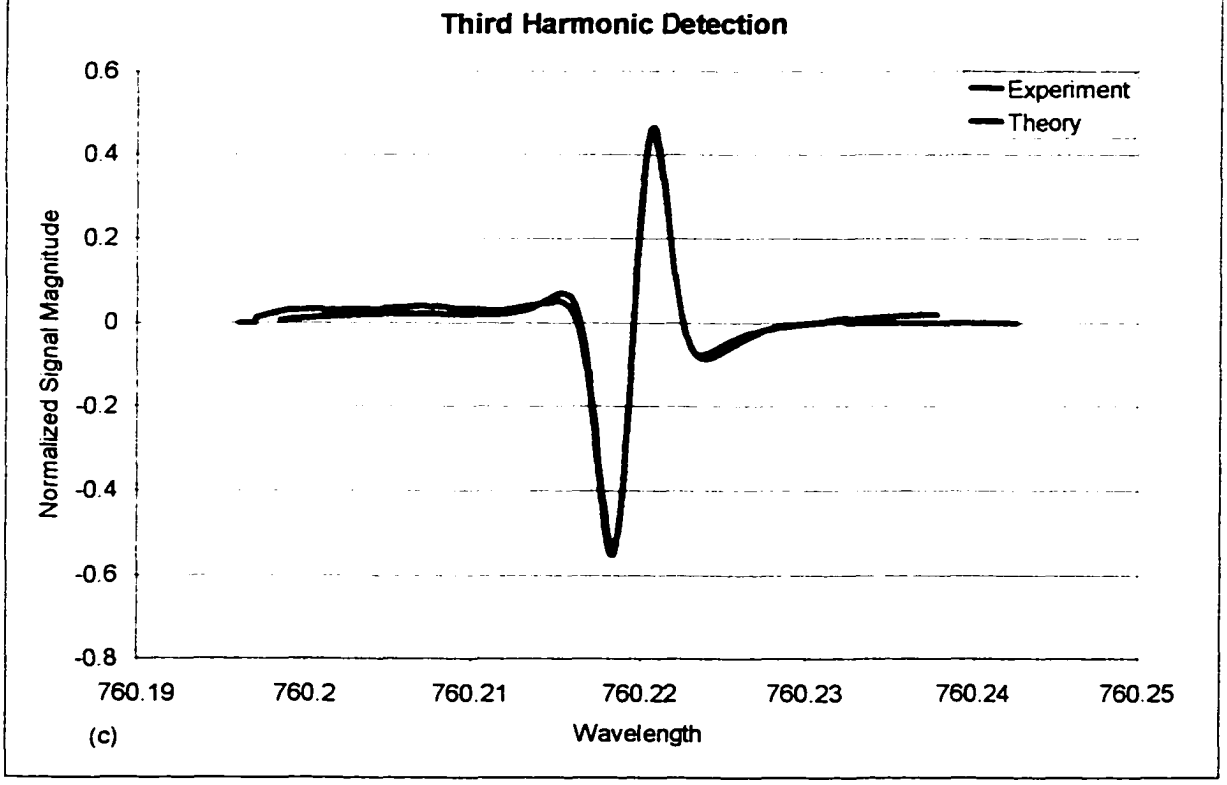

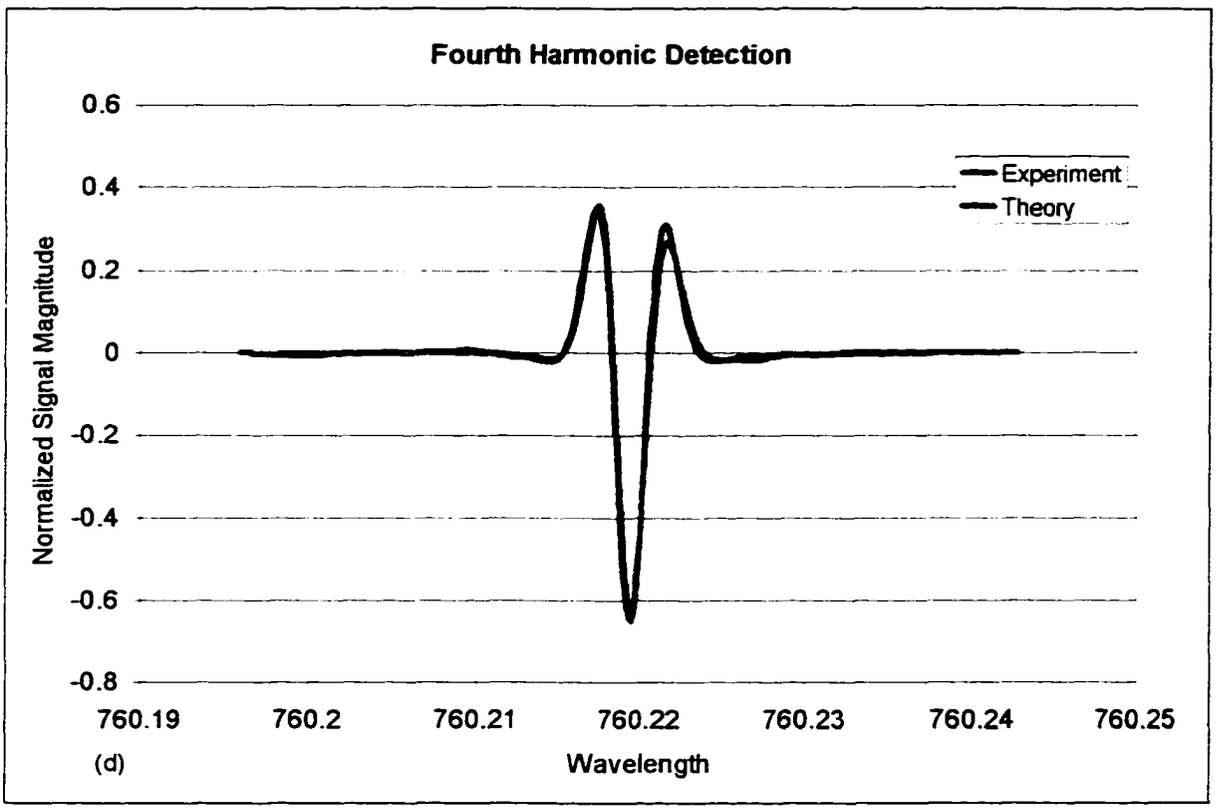

Figure 15(a-d) Experimental and theoretical results for harmonic detection signals, N=1-4, for the RR(15,15) absorption line. Experiment made with Plexiglas blank inside the multipass cell (set for ten passes).

Figures 15(a) through (d) show experimental signals with matching theoretical calculations, which include Fabry-Perot fringing. Note that the first harmonic signal is very distorted, and it would be impossible to theoretically match the experimental data without the incorporation of Fabry-Perot fringing. As predicted in previous chapters, the SFNR increases when going to higher harmonics. This is visually seen in harmonics 1 through 3. The change in SFNR between third and fourth harmonics is not directly measurable due to the under-modulation seen in fourth harmonic. This is also seen in Figure 14(d) where under-modulation was a factor.

Just as it is for the results shown in Figure 14, in order to obtain the matches in Figures 15(a-d), all of the parameters must be correct or there is no hope for a match that

works for all harmonics. These parameters include d, n, and θ. The thickness of the blank, d, was measured with calipers accurate to 0.005 in., which corresponds to an accuracy of two percent. The index of refraction, n, for Plexiglas was taken to be 1.5. By changing the angles by less than two percent, it is possible to alter the calculation of the transmission function of the etalon enough to allow for either a good match, or a match that has error on the order of 90%. Due to the dependence of the etalon's transmission function on θ, and the number of passes the laser made though the etalon, the ability to get a perfect match is extremely difficult because each parameter must be accurate in order to calculate a good theoretical match. The excellent agreement between theory and experiment allows one to have a high degree of confidence in the theory and the measurements.

4.2 (a.3) Rotated Intracavity Etaloning Element

A similar experiment to that in Section 4.2 (a.2) was conducted, but this time the blank was tilted with respect to the optical axis. This new arrangement produced considerably different experimental fringe patterns. This was used to advantage in that it allowed another set of independent measurements to be made on the line RR(15,15). These measurements were done in the same manner as those described previously in section 4.2 (b).

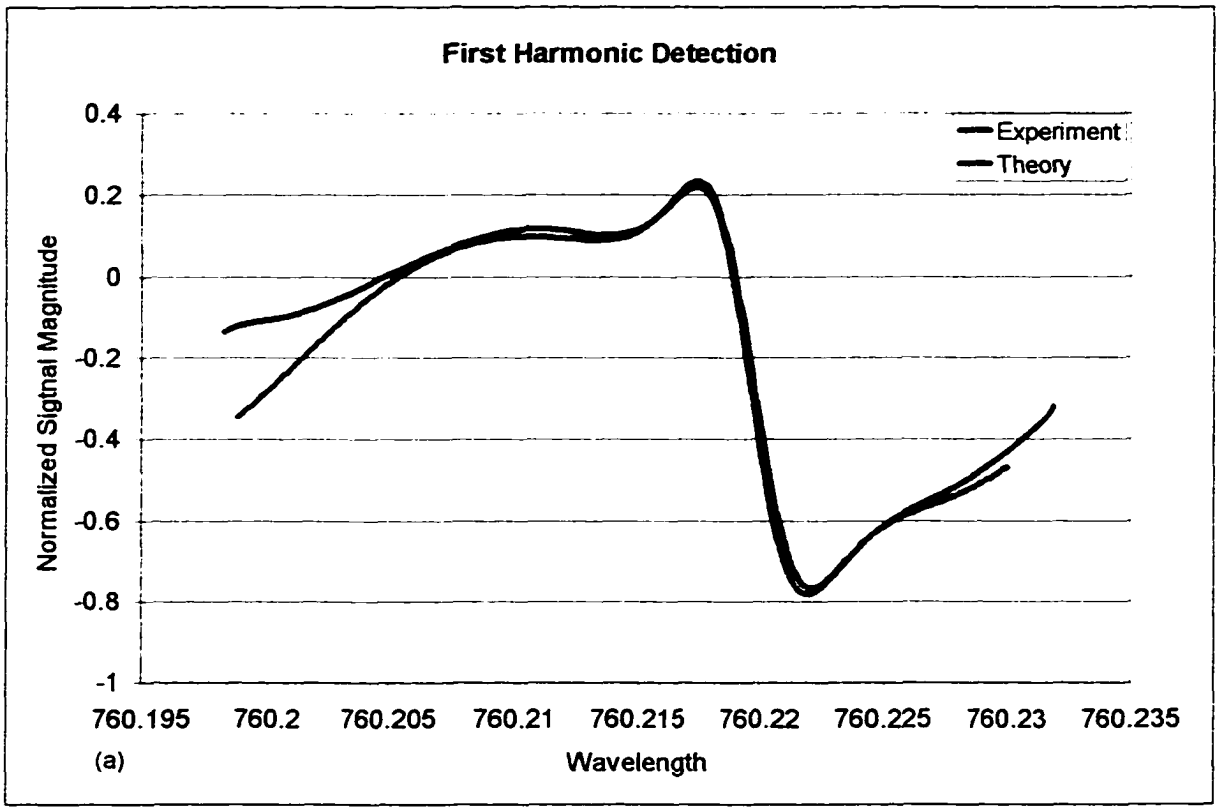

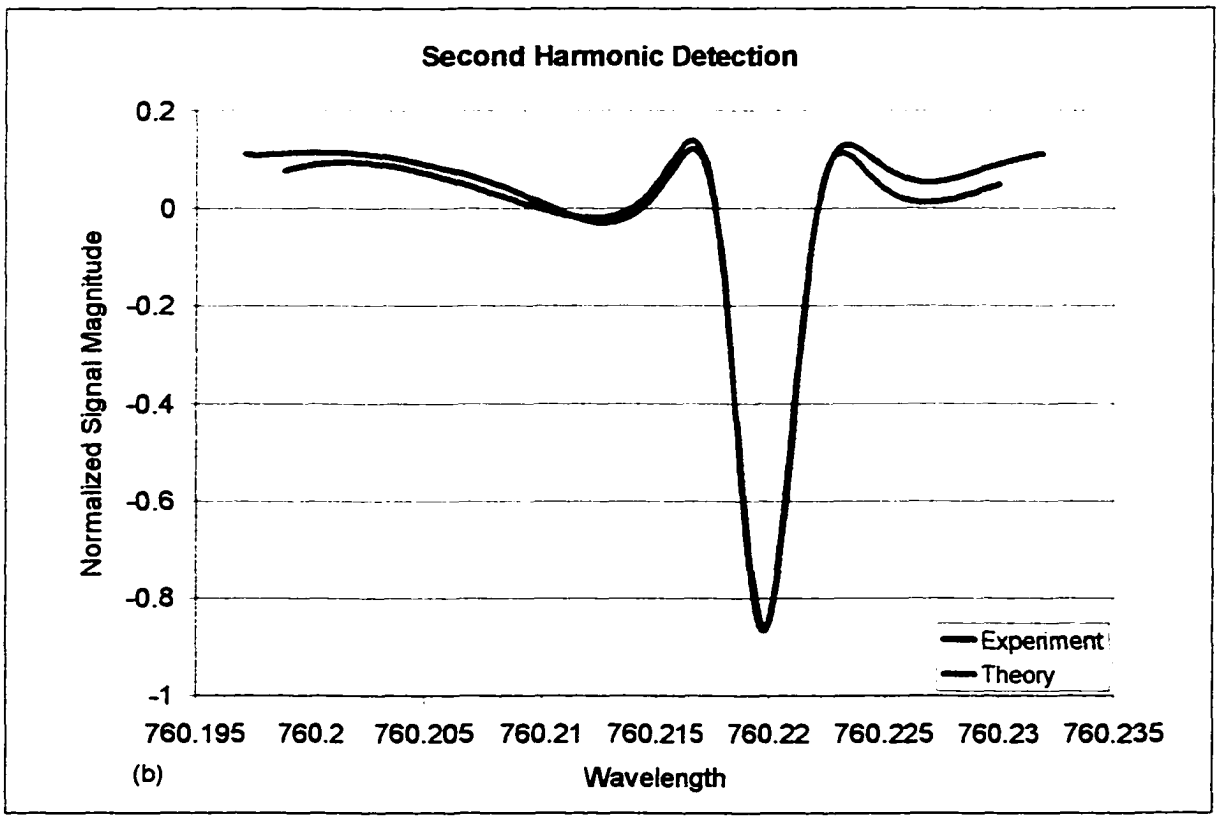

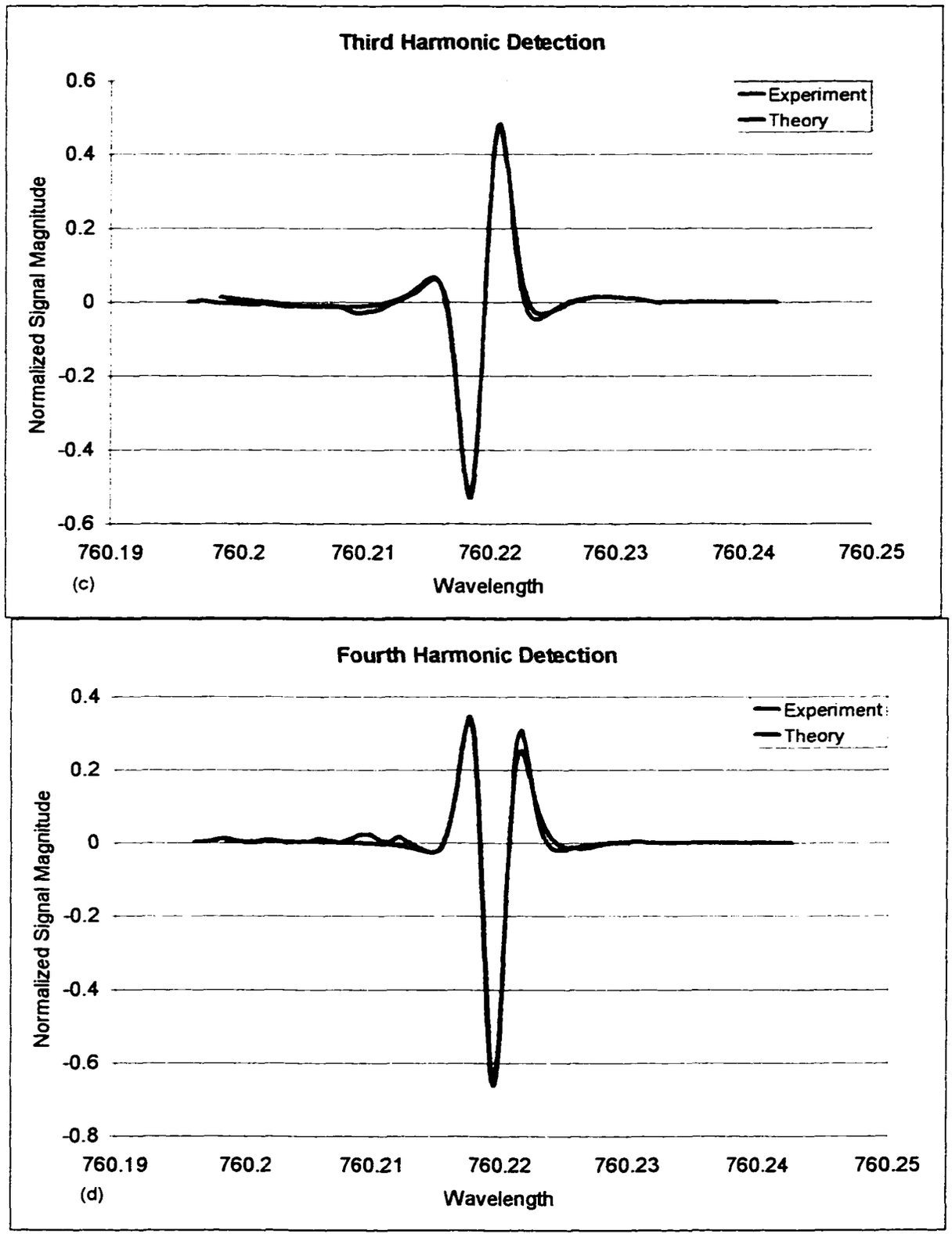

Figure 16(a-d) Experimental and theoretical results for harmonic detection signals, N=1-4, for the RR(15,15) line. Experiment made with Plexiglas blank inside the multipass cell (set for ten passes).

Figures 16(a-d) are plots of experimental data and theoretically calculated matches for first through fourth harmonic detection orders. The line parameters used are exactly the same as those used in Figures 15(a) through (d). The measurement of the angle α was increased by one degree for all ten passes. As for the results shown in Section 4.2 (b), the values of the angles used in the computation were all within two percent of the measured values. Therefore, the actual change in α was 1 degree $\pm 2\%$ from the original measured values. The theoretical calculations are very close to the experimentally obtained curves. The errors are due to the complexity in matching ten angles corresponding to the ten passes through the etalon. The ten-pass system was used to amplify the effects of the fringing to help demonstrate the power in modeling the fringe to obtain the line parameters.

As in the previous set of figures for the first fringe pattern, the SFNR increases with harmonic order with an apparent maximum in third harmonic, N=3. This is partially due to the etalon itself. As seen in chapter three, the parameters used lend themselves to a large SFNR ratio in third harmonic. In fourth harmonic one expects an even larger SFNR, however, this is not directly measurable due to the increase in noise from other sources which become visible with the reduction in the magnitude of the absorption signal that is a result of making a measurement at the fourth harmonic. Also, there is evidence of distortion produced by under-modulation in fourth harmonic.

4.2 (b) Experimental Measurements of the RQ(15,16) Absorption Line Using a Six Pass Multipass Cell

The results from a study of the effects that the number of passes the laser beam makes through an optical blank (etalon), and how the number of passes affects the overall

transmission function of the detected signal is presented in this section. The procedure for this experiment is identical to the previous experiments in Section 4.2 (a) except the separation between the mirrors of the multipass cell was changed to provide six passes through the cell. Three experiments were then conducted with this arrangement. One experiment was made without an etalon to be used as a baseline for modeling the absorption signal and as a reference point for measuring the etaloning. The second experiment was conducted with the Plexiglas blank inserted inside the multipass cell normal to the optical axis. This allowed a measurement of an increase in the etaloning while keeping the absorption path length approximately the same; the difference in path length is four times the thickness of the Plexiglas blank. The results from these experiments are shown below in Sections 4.3 (a-b).

4.2 (b.1) Baseline Measurement without Etaloning Element

The following measurements were made of line RQ(15,16) in the oxygen A-band with a six pass multipass cell without an optical blank. The following set of figures show experimental and theoretically calculated results for the absorption line using the parameters listed in Table 1 in Section 4.4. The results below show good agreement between the experimentally and theoretically obtained line profiles. The good agreement is maintained throughout all four harmonic detection orders and therefore gives us confidence in the parameters used in calculating the theoretical plots.

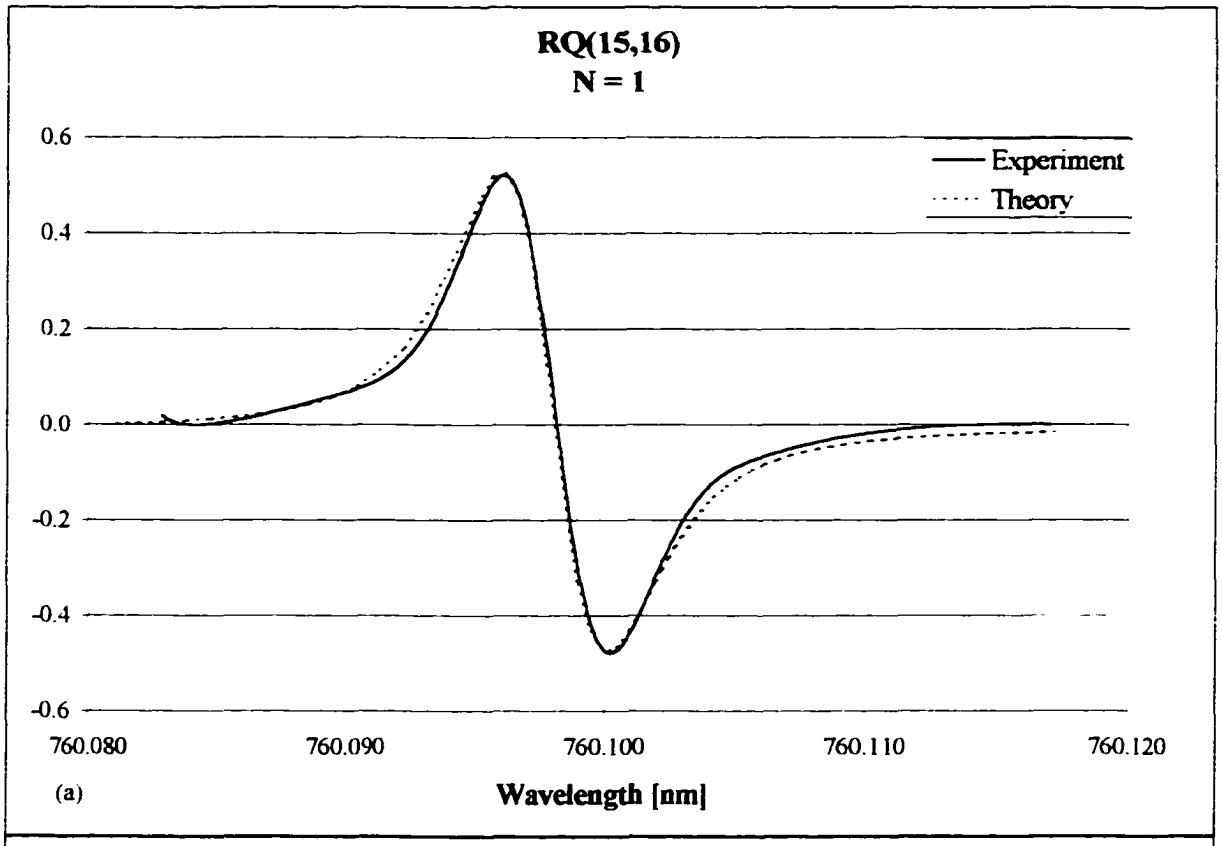

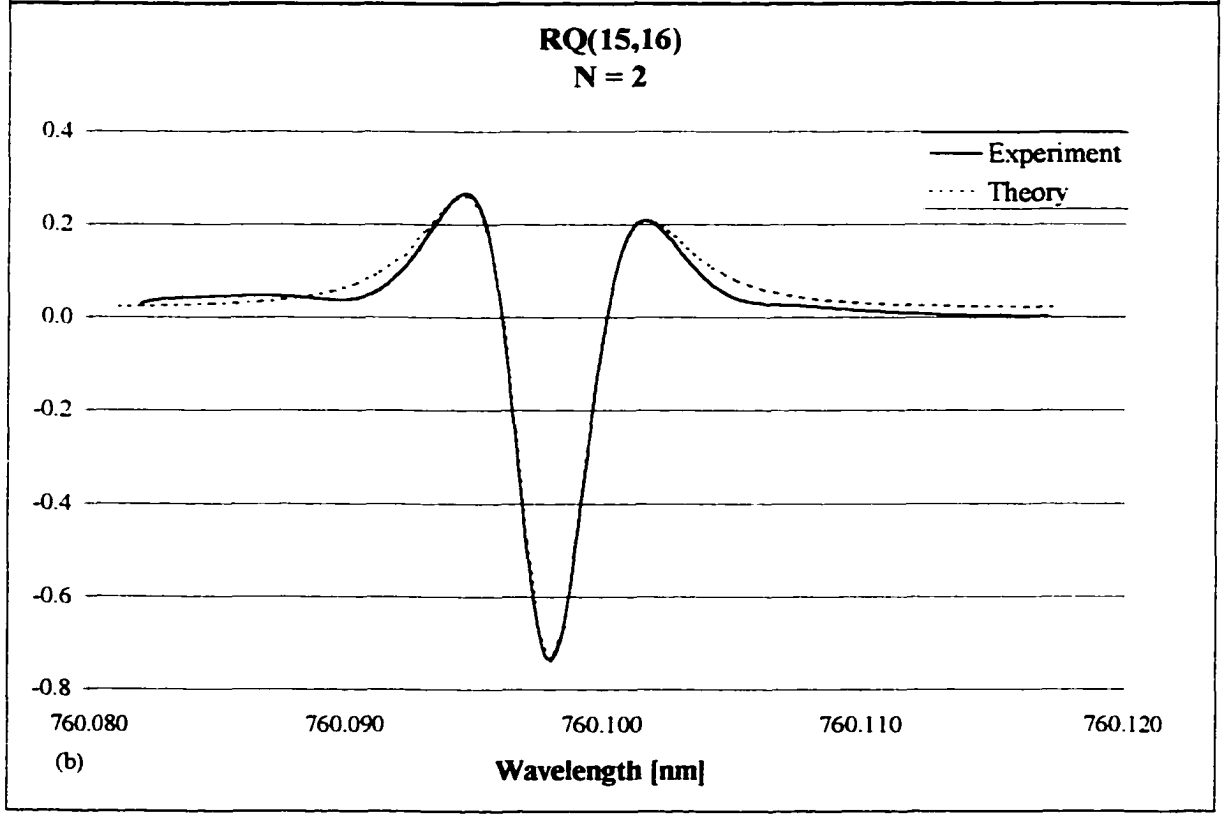

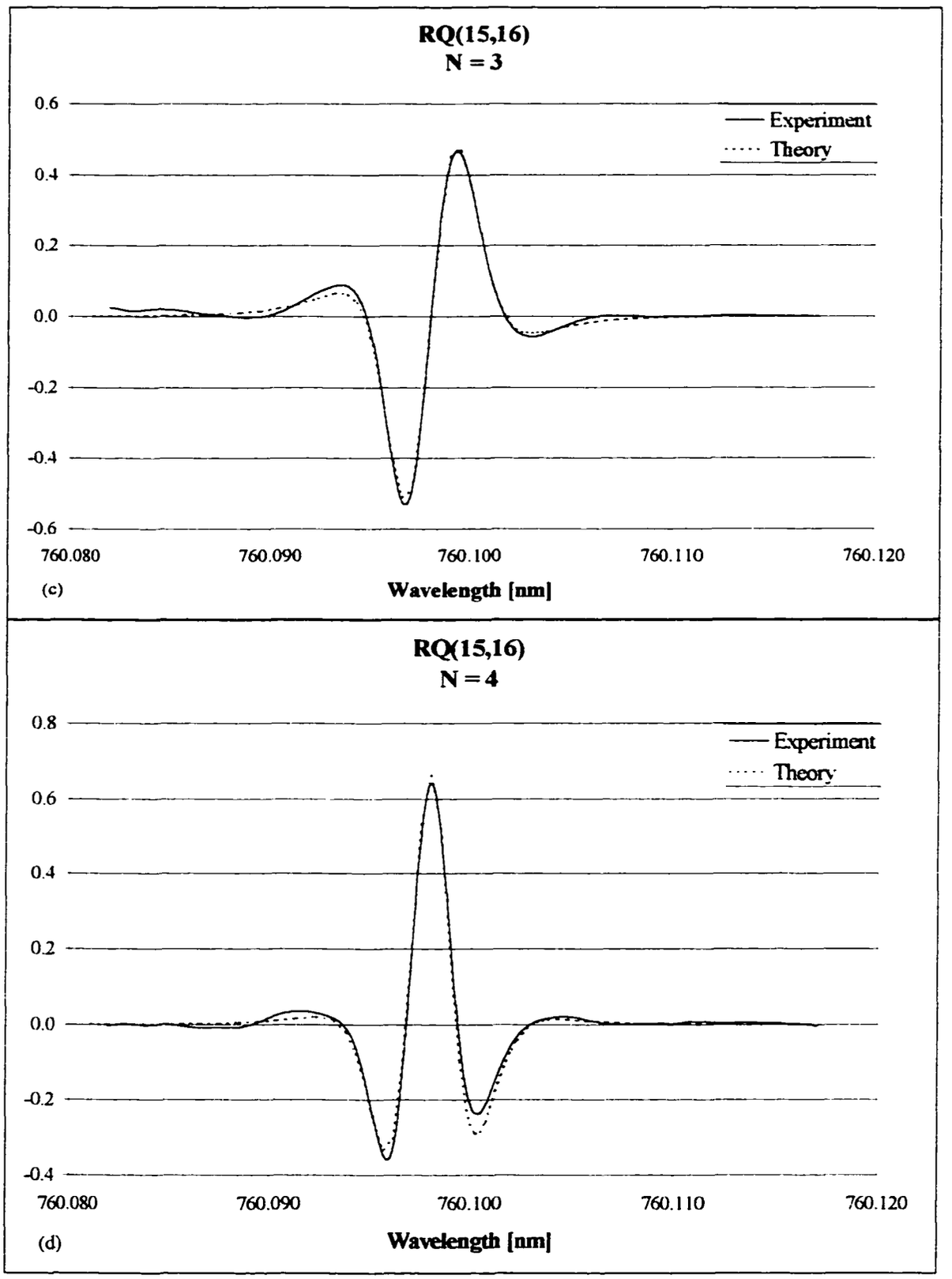

Figure 17 (a-d) Experimental and Theoretical Results for harmonic detection signals, N=1-4, of RQ(15,16) without fringing (Baseline measurement).

4.2 (b.2) Intracavity Etaloning Element Normal to Optic Axis

This section shows the effects of an etalon on the absorption signal for a six-pass multipass cell with the fringing element inside the cell, yielding six passes through the etalon. The results show the trend seen in Section 4.2 (a) in that the fringing greatly distorts the absorption signal. These results show all of the same trends as the previous set of figures in Sections 4.3 (b-c). The effects of fringing seem to be eliminated by the third harmonic detection order, N=3. On the short wavelength side of Figure 18(c), it is noticed that the experimental signal and the theoretical signal do not match. This is due to large second order non-linearities in the current ramp that.

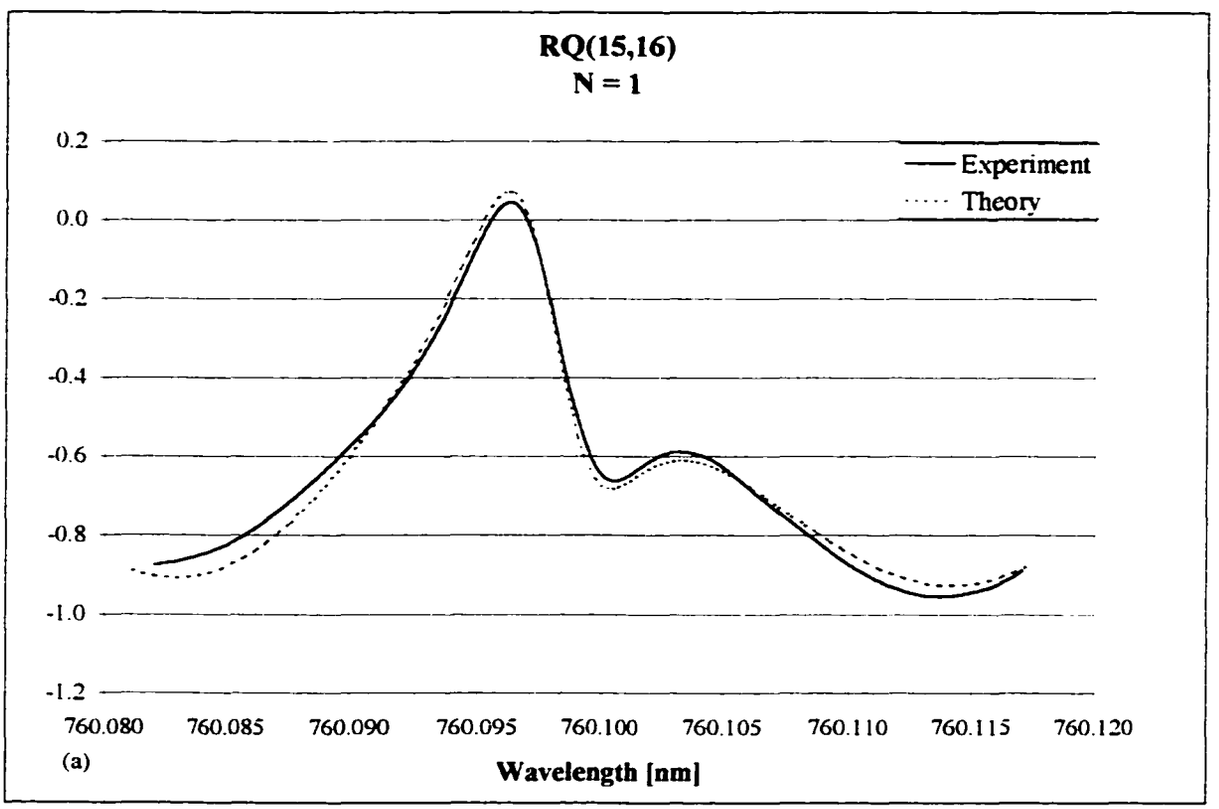

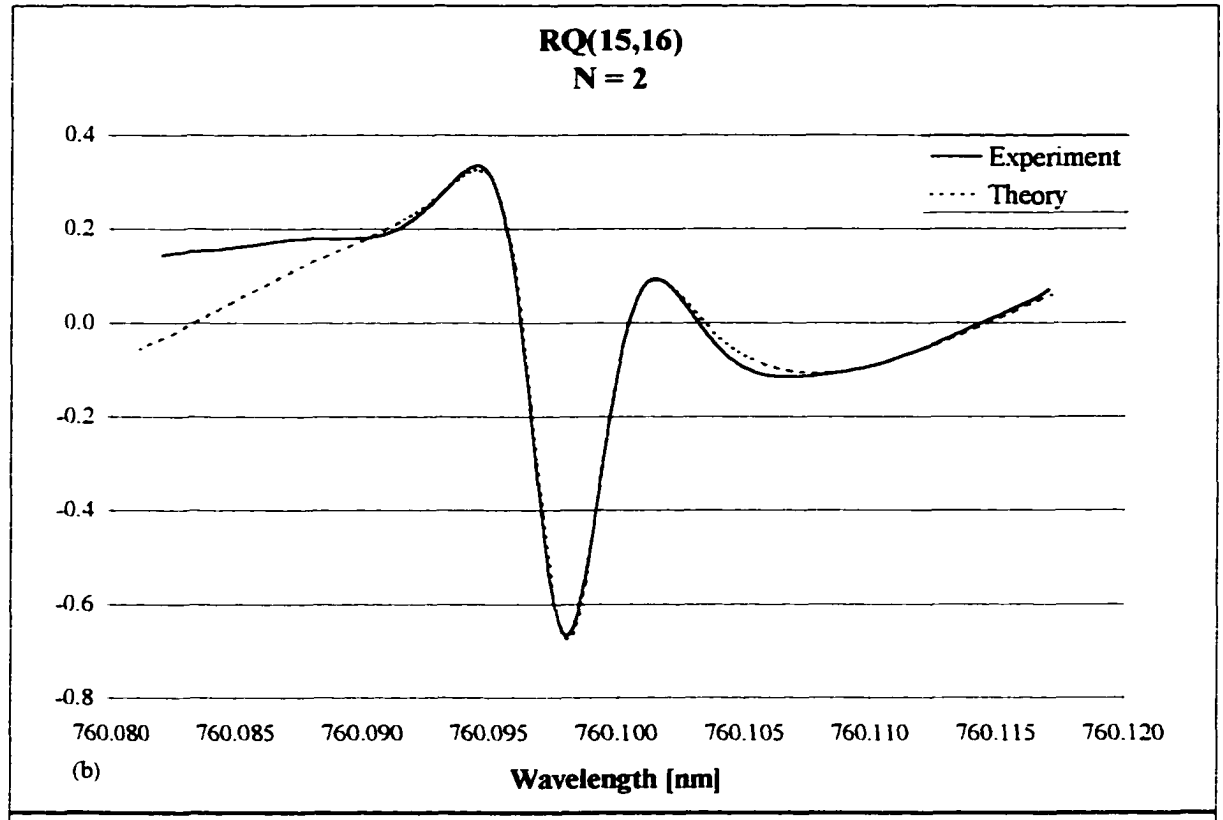

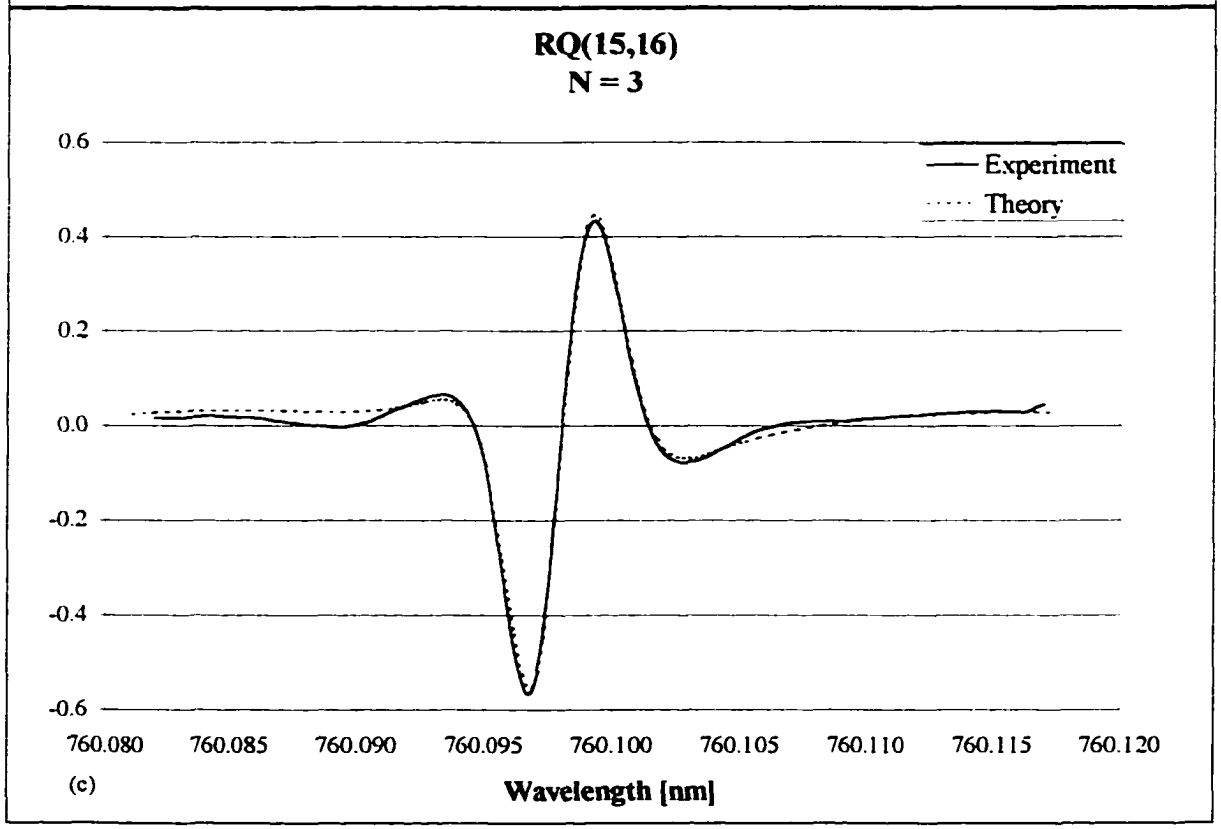

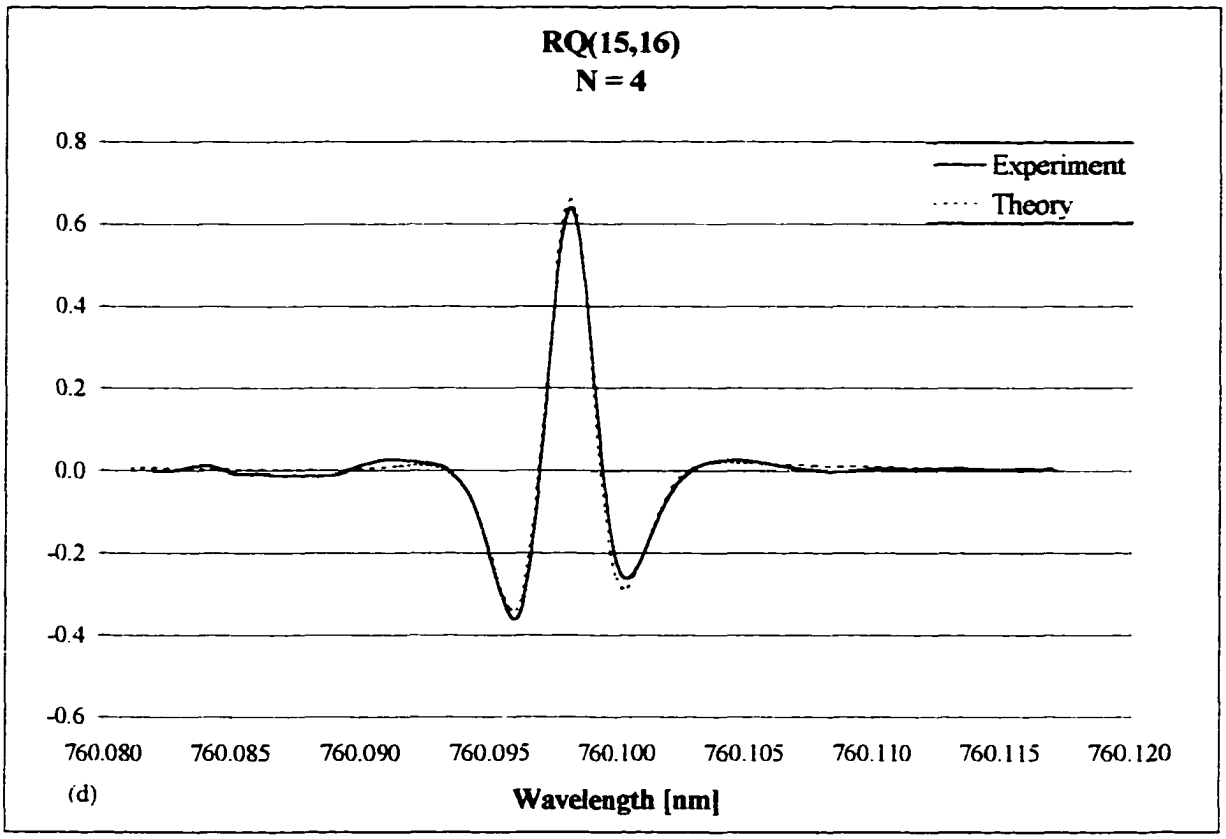

Figure 18 Experimental and Theoretical results for harmonic detection signal, N=1-4, of the RQ(15,16) absorption line with etaloning element.

4.3 Comparison of Measured Line Parameter Values with Those in Hitran '96

Note that the theoretical fits to the experimental results obtained for the experiments for the RR(15,15) and RQ(15,16) lines, shown in Figures 14 through 18 have been obtained by using the values indicated in Table 1 below.

Table 1 Measured values of O_2 A-band line parameters and comparison to HITRAN '96 values.

	Values used thesis			HITRAN '96		
Line	line strength [$cm^2mol^{-1}cm^{-1}$]	Linecenter [nm]	Line Width [cm^{-1}]	line strength [$cm^2mol^{-1}cm^{-1}$]	Linecenter [nm]	Line Width [cm^{-1}]
RR(15,15)	4.36e-24	760.2109(9)	0.086	4.36e-24	760.2151(0)	0.1018
RQ(15,16)	4.79e-24	760.0990(0)	0.104	4.79e-24	760.0937(0)	0.0996

Table 2 Percent difference between the values used in this work and HITRAN '96.

Parameter	Percent Difference	Percent Difference
Line	RR(15.15)	RQ(15.16)
Line strength	0*	0*
Linecenter	5e-4	7e-4
Line Width	13	4.42

*No change was required of HITRAN's absorption cross-sections for fits. However there is assumed error on the order of ΔT_{FP} as defined in Appendix A.

4.4 DISCUSSION

The experimental results shown in this chapter demonstrate the ability to model the fringing in an experiment and the usefulness of that modeling. Without the knowledge of the effects of fringing, the experimental results shown above would be of little value. Only by modeling the fringe can the experimental signal be matched to theory at the lower harmonic detection orders and in this way the absorption signal can be obtained, inspite of the large fringing. The experiments also show the importance of higher harmonic detection, and the ability to overcome Fabry-Perot fringing by going to higher harmonic detection. This is the first time that the method of higher harmonic detection has been used to eliminate Fabry-Perot etaloning in a wavelength modulation experiment. The technique has clear advantages over the method that employs asynchronous jittering of the offending element [1].

The results obtained in this work also show that one can, with proper modeling, account for Fabry-Perot etaloning that occurs in many wavelength modulation experiments. This ability allows one to identify the element that causes fringing. Even if this element cannot be eliminated, the modeling technique described allows one to obtain useful results that might not be possible otherwise.

Note that the values shown in Table 1 that were used provided the fits displayed for all the detected harmonic orders measured (N=1, 2, 3, 4). Hence, the values given in that table can be stated with a large amount of confidence. Note also that while absolute linecenters were not measured directly in this work, the fact that the matches shown in Figures 14 through 18 occur even in the presence of fringing, gives us confidence in the absolute cross-sections shown in Table 1. This follows from the fact that, as seen from Equation (3.10), the inclusion of the etaloning transmission coefficient serves as a check for the value of the absorption line strength.

Therefore, to the extent that the etalon's transmission in known experimentally, one has confidence in the values of the absolute line strengths given in Table 1. Note that the values of the line parameters measured have been obtained by effectively six independent measurements of the RR(15,15) line (Figures 15 and 16; N=1, 2, and 3 for two different orientations of the blank), and by three independent measurements for RR(15,16).

CHAPTER V

CONCLUSIONS

While wavelength modulation spectroscopy is a very useful non-intrusive measuring technique, the results presented in this thesis show that the usefulness of this tool might be limited by etaloning effects. We have shown how these etaloning effects may be accounted for, and how in many situations, the deleterious effects of Fabry-Perot fringing may be minimized.

We have shown that if the etalon's parameters (n, d, and θ) are known, then the line parameters can be determined absolutely from the modeling of both the etaloning and the absorption line. In this case (with the etalon's parameters known), the transmission function is known and provides a reference that can be used to fit the absorption line. This will allow for only a small set of line parameters that will produce a match between theory and experiment. Therefore, the error in the line parameters can be reduced to the errors in the calculation of the etalon by fitting theory with experiment.

An important parameter studied in this thesis was the ratio of the quality factors of the etalon to that of the line. This parameter, q, was important in determining the effect of increasing harmonic detection order on fringing. It was found that for q less than 0.1, the fringing could be eliminated by going to higher harmonics; usually the third harmonic was sufficient. It was also found that for systems where q was equal to or greater than 1, the fringing would dominate the signal at higher harmonics and SFNR would deteriorate rapidly. For values of q between 0.1 and 1, the fringing was never eliminated at higher harmonics, where fourth harmonic was the limit in the study. However the amount of residual fringing depended on the value of q and how the absorption line's and etalon's

transmission functions overlapped. Hence, the SFNR is not always an accurate measurement of the amount of fringing in an experiment. If the overlap occurred near a peak, then the apparent distortion was in the magnitude of the signal and line was more easily recognizable. On the other hand, if the overlap occurred on the slope of the etalon's transmission function, the shape of the absorption signal was much more greatly distorted.

If higher harmonic detection is used to reduce Fabry-Perot fringing, then one must be able to estimate the optimum harmonic detection order that needs to be used to eliminate the fringing. For all the cases we examined this optimum harmonic detection order is greater than the commonly used second. For most of the cases investigated in this thesis, the "optimum" detection order for reducing fringing was the third. The signal to noise ratio in fourth harmonic could be increased by increasing the modulation amplitude, which effectively increases the signal magnitude. In our case, constant modulation amplitude was used for all the observed signals per experiment, and under the conditions used to make the measurements, third harmonic was optimum.

A possible use for higher harmonic detection for the elimination of Fabry-Perot fringing arises in measuring extremely weak absorption lines. Theoretically, it is conceivable that a weak line could be totally overwhelmed by fringing in first and even second harmonic detection. The line could be measured the harmonic detection order is increased to third or even fourth.

LIST OF REFERENCES

[1] J.A. Silver, A. Stanton, *Applied Optics*, **27**, 1914-1916, (1988).

[2] A. Fried, et al., *Applied Optics*, **29**, 900-902, (1989).

[3] A.N. Dharamsi, A.M. Bullock, *Applied Physics Letters*, **69**, 22-24, (1996).

[4] A.M. Bullock, P.C. Shea, A.N. Dharamsi, *IEEE Lasers and Electro-Optics Society 1997 Annual Meeting*, **2**, 550, (1997).

[5] A.N. Dharamsi, Y. Lu, *Applied Physics B*, **62**, 273-278, (1996).

[6] K.T. Ritter, T.D. Wilkerson, *Journal of Molecular Spectroscopy*, **121**, 1, (1987).

[7] A.N. Dharamsi, A.M. Bullock, P.C. Shea, *Applied Physics Letters* (Scheduled to appear June 15, 1998).

[8] "Physics of weakly ionized Gases," B.M. Smirnov, Springer-Verlag, New York, (1985).

[9] "Molecular spectra and Molecular Structure: I. Spectra of Diatomic Molecules," G. Herzberg, D. Van Nostrand Company Inc., New York, (1950).

[10] "Laser Electronics," J.T. Verdeyen, Prentice-Hall, Inc. New Jersey, (1995).

[11] A.N. Dharamsi, *Applied Physics D*, **29**, 540-549, (1996).

[12] "Introduction to Optical Electronics" A. Yariv, Holt, Rinehart and Winston, (1976).

[13] G. V. H. Wilson, *Journal of Applied Physics*, **34**, 3276, (1963).

APPENDIX I

ACCURACY OF MEASURED PARAMETERS

In order to estimate the accuracy of the results obtained, it is necessary to examine how the error in the measurements of the Fabry-Perot etalon's parameters propagate through the calculation of the etalon's transmission function. The errors in the measured values of the laser beam location on the multipass cell's mirrors together with accuracies in the measurements of the thickness and index of refraction are given in Table 3 below.

Table 3 Errors in measurements of the Fabry-Perot etaoln's parameters.

Parameter	Value	Accuracy	Percent Error
x_1	111.5 [mm]	± 1 [mm]	0.89%
y_1	56 [mm]	± 1 [mm]	1.8%
z_1	0 [mm]	± 0 [mm]	-
x_2	200 [mm]	± 1 [mm]	0.5%
y_2	85 [mm]	± 1 [mm]	1.2%
z_2	675 [mm]	± 10 [mm]	1.5%
d	.785 [cm]	± 0.023 [cm]	3%
n	1.5	± 0.05	3%

The parameters x_1, y_1, z_1, x_2, y_2, z_2 are the locations of the spots on the mirrors caused by the reflection of the laser beam and are needed to calculate the angles used for calculating the transmission function of the Fabry-Perot etalon. The values in the table are for two endpoints of a representative ray. The equation for calculating the angle α, the eternal angle of incidence is given by Equation (A1.1) below.

$$\cos(\alpha) = \frac{U \bullet V}{\|U\|\|V\|}, \tag{A1.1}$$

where V is the unit vector normal to the optical blank, $\hat{z}$.

This equation simplifies to Equation (A1.2).

$$\cos(\alpha) = \frac{(z_2 - z_1)}{\sqrt{(x_2 - x_1)^2 + (y_2 - y_1)^2 + (z_2 - z_1)^2}} \tag{A1.2}$$

The error in cos(α) was found by taking the partial derivatives with respect to all six parameters and multiplying them by the error in that parameter. The six errors were then added to give the total fractional error in cos(α).

$$\frac{\Delta(\cos\alpha)}{\cos\alpha} = \frac{1}{\cos\alpha}\left(\frac{\partial(\cos\alpha)}{\partial x_1}\Delta x_1 + \frac{\partial(\cos\alpha)}{\partial y_1}\Delta y_1 + \frac{\partial(\cos\alpha)}{\partial z_1}\Delta z_1 + \frac{\partial(\cos\alpha)}{\partial x_2}\Delta x_2 + \frac{\partial(\cos\alpha)}{\partial y_2}\Delta y_1 + \frac{\partial(\cos\alpha)}{\partial z_2}\Delta z_2\right) \tag{A1.3}$$

Using Equations (A1.4), (A1.5) and equations analogous to (A1.3) gives the total error in the Fabry-Perot transmission function.

$$\theta = \arcsin\left[\frac{1}{n}\sin(\arccos(\alpha))\right] \tag{A1.4}$$

$$T_{FP} = \frac{1}{1 + \rho\sin^2\left(\frac{2\pi nd\cos(\theta)}{\lambda}\right)} \tag{A1.5}$$

This total error in the transmission function was calculated with respect to n, d, and θ. Using the values shown in Table 3 above, the errors in α, θ, and in the transmission function were calculated. These are shown in Table 4.

Table 4 Values and percent error for calculated etalon parameters.

Parameter	Value	Accuracy	Percent Error
α	0.1371 [rad]	0.002 [rad]	1.46%
θ	0.09124 [rad]	0.0013 [rad]	1.46%
ΔT_{FP}	0.9825	0.0167	1.70%

The error in calculation of the peak in the transmission function for the etalon was also calculated. This was done by solving for the peak in the transmission function and taking the partial derivatives with respect to n, d, and θ. The equation for the peaks in the Fabry-Perot etalon's transmission function is given below in Equation (A1.6b).

$$\frac{\partial}{\partial\delta}\left(\ln\left[1+\rho\sin^2\left(\frac{\delta}{2}\right)\right]\right)=0 \tag{A1.6a}$$

$$\frac{2\pi nd\cos(\theta)}{\lambda}=m\pi \tag{A1.6b}$$

To calculate the error in the peak, the partial of λ_{peak} with respect to n, d, and theta must be taken. To calculate an appropriate error, the correct value of m must be used. m corresponds to the peak in the transmission function closest to linecenter of the absorption line and is given by

$$m=\text{IntegerPart}\left[\frac{2nd\cos(\theta)}{\lambda_{oline}}\right]. \tag{A1.7}$$

This value for m is calculated, and the number is substituted into the equation below from with the error in the λ_{peak} for the transmission function is calculated. With the etalon parameters in Table 3, and a linecenter of the absorption line of 760.000 nm, m has the value 61712.

In order to estimate the accuracy of the linecenter measured and specified in Table 2, one needs to estimate the error in the value of λ_{peak} (λ_{peak} being the peak in the Fabry-Perot transmission function immediately to the lower wavelength side of the absorption line). This follows because it has been found during the course of this work that in order to get a match between theoretical and experimental results, the separation between the

absorption line (λ_{oline}) and λ_{peak} plays a critical role. Hence, in order to find $\Delta\lambda_{oline}$ one needs to calculate $\Delta\lambda_{peak}$ from Equation (A1.6b)